Geochemistry, Geophysics, Geosystems®

RESEARCH ARTICLE
10.1029/2025GC012745

Radiolysis and Fe-Biotite Alteration: Questioning the Origin of H_2-Bearing Fluid Inclusions in the Yorke Peninsula Granites, South Australia

Ugo Geymond[1,2], Dan Lévy[1], Julien Bourdet[3], Isabelle Martinez[1], Olivier Sissmann[2], Sidonie Revillon[4], Rayanne Gormit[5,6], Sylvain Bernard[7], Pierre-Henri Blard[8], David Bekaert[8], Jimmy Daynac[9], Stephan Borensztajn[1], Se Gong[10], Clément Herviou[1], Emanuelle Frery[3], and Isabelle Moretti[5,6]

[1]IPGP, CNRS—UMR 7154, Université Paris Cité, Paris, France, [2]IFP Energies Nouvelles, Rueil-Malmaison, France, [3]CSIRO Energy, Kensington, WA, Australia, [4]Sedisor, Plouzané, France, [5]ISTeP, CNRS—UMR 7193, Sorbonne Université, Paris, France, [6]LFCR, CNRS—UMR 5150, Université de Pau et des pays de l'Adour, Pau, France, [7]MNHM, IMPMC, CNRS—UMR 7590, Sorbonne Université, Paris, France, [8]CRPG, CNRS—UMR 7358, Université de Lorraine, Vandoeuvre-les Nancy, France, [9]LPG, CNRS—UMR 6112, Le Mans Université, Le Mans, France, [10]CSIRO Energy, Lindfield, NSW, Australia

Key Points:

- H_2 and He were measured in Hiltaba granites, suggesting this basement lithology as a source for gases found in shallow sedimentary units
- Radiolysis inferred as the main H_2 source, with no evidence that Fe-biotite alteration contributes to H_2 generation in the studied sample
- Last fluid circulation was estimated at >370 Ma, implying diffusive migration as the main driver of H_2 and He anomalies in shallow sediments

Supporting Information:

Supporting Information may be found in the online version of this article.

Correspondence to:

U. Geymond,
geymond@ipgp.fr

Citation:

Geymond, U., Lévy, D., Bourdet, J., Martinez, I., Sissmann, O., Revillon, S., et al. (2026). Radiolysis and Fe-biotite alteration: Questioning the origin of H_2-bearing fluid inclusions in the Yorke Peninsula granites, South Australia. *Geochemistry, Geophysics, Geosystems*, *27*, e2025GC012745. https://doi.org/10.1029/2025GC012745

Received 21 OCT 2025
Accepted 1 MAR 2026

Author Contributions:

Conceptualization: Ugo Geymond, Isabelle Martinez, Isabelle Moretti
Formal analysis: Ugo Geymond, Dan Lévy, Julien Bourdet, Olivier Sissmann, Sidonie Revillon, Rayanne Gormit, Sylvain Bernard, Pierre-Henri Blard, David Bekaert, Jimmy Daynac, Stephan Borensztajn, Se Gong, Clément Herviou
Funding acquisition: Emanuelle Frery, Isabelle Moretti

Abstract Multiple drillings in the Yorke Peninsula, South Australia, recently confirmed the presence of natural hydrogen (H_2) in shallow sedimentary units. While radiolysis and Fe-oxidation in the basement are potential generation mechanisms, their respective contributions remain unconstrained. This study investigates the H_2-generation potential of Fe-rich Hiltaba Suite granites (~1.5 Ga) through petrographic analyses of a basement drill core collected near H_2 occurrences. Fluid circulation, a prerequisite for both radiolysis and Fe-oxidation, is evidenced by feldspar sericitization and fluid inclusions. Raman spectroscopy and sample crushing analyses reveal H_2 (0.46 mmol/kg_{rock}) and He (0.70–0.88 µmol/kg_{rock}), suggesting that the Hiltaba granites contribute to the gas budget observed in the overlying sedimentary units. He isotopic analyses from bulk granites yield $^3He/^4He$ ratios from 0.0003 to 0.0056 Ra, indicating a crustal He origin and a radiolytic H_2 generation. A combination of SEM, TEM, EPMA and STXM analyses showed that biotite chloritization did not involve Fe-oxidation. As biotite is the only primary Fe-bearing mineral affected by alteration, this rules out any significant contribution of Fe oxidation to H_2 generation. Geothermometric calculations indicate that the last fluid circulation event occurred at 300–400°C, implying that the system last opened dynamically at least 370 Ma ago. Consequently, we propose that diffusive migration of H_2 and He from the basement accounts for the gas fluxes in the sedimentary cover. This study represents a first step toward understanding subsurface H_2 and He generation in the Yorke Peninsula and highlights the Hiltaba Suite's potential to source H_2 and He over geological timescales.

Plain Language Summary Natural hydrogen is an emerging potential clean energy resource, and recent discoveries in South Australia have driven strong interest. In the Yorke Peninsula, shallow sedimentary units contain substantial amounts of co-occurring hydrogen (H_2) and helium (He). The genetic processes leading to this subsurface gas blends are not fully understood and constrained, and there are still more to be debated. Two main possibilities exist, each involving water-rock interactions: water molecule reduction associated with iron oxidation, and water molecule breakdown induced by the natural radioactive decay in rocks (that also produces helium). To test these ideas, we studied a drill core from granites constituting the basement near the H_2-He discoveries. We reveal clear evidence of fluid circulation coupled to H_2 and He measurements within the granite, validating that the studied rock participates in the H_2 and He budget in the region. The He composition indicates that radioactivity plays a crucial role in producing H_2. In contrast, we found no signs that iron oxidation contributed. Additional interpretations suggest that, over time, these gases could have slowly migrated upward to the shallow rocks where H_2 and He are now detected. This finding highlights the importance of granites as potential natural H_2 sources worldwide and provides valuable insights for future exploration in South Australia.

1. Introduction

On the Yorke Peninsula, South Australia, an oil and gas exploration drillhole named Ramsay Oil Bore was drilled one century ago (Ward, 1933). During operations, elevated H_2 concentrations (76%–84% after correction for air contamination) were detected at the wellhead (Whitcombe et al., 2024), but the origin of this gas remained

Investigation: Ugo Geymond, Dan Lévy, Julien Bourdet, Olivier Sissmann, Sidonie Revillon, Rayanne Gormit, Sylvain Bernard, Pierre-Henri Blard, David Bekaert, Jimmy Daynac, Stephan Borensztajn, Se Gong, Clément Herviou
Resources: Ugo Geymond, Isabelle Martinez, Isabelle Moretti
Supervision: Ugo Geymond, Isabelle Martinez, Emanuelle Frery, Isabelle Moretti
Writing – original draft: Ugo Geymond
Writing – review & editing: Ugo Geymond, Julien Bourdet, Isabelle Martinez, Olivier Sissmann, Sidonie Revillon, Sylvain Bernard, Pierre-Henri Blard, David Bekaert, Jimmy Daynac, Clément Herviou, Emanuelle Frery, Isabelle Moretti

unexplored. Recent drillings conducted in 2023 by Gold Hydrogen Limited in the same area confirmed the presence of world-class H_2 anomalies reaching up to 86% (air-corrected) in the sampled gas, along with He concentrations of up to 17.5% (air-corrected) (see www.goldhydrogen.com.au/ramsay-project/).

The co-occurrence of H_2 and He has been documented in multiple locations worldwide, for example, in the Canadian and Fennoscandian shields (Sherwood Lollar, Frape, Fritz, et al., 1993; Sherwood Lollar, Frape, Weise, et al., 1993) and in the Witwatersrand Basin, South Africa (Karolytė et al., 2022; Onstott et al., 2006; Sherwood Lollar et al., 2007). Such a gas blend is commonly attributed to radiolysis driven by water-rock interactions within Precambrian basement rocks enriched in radioactive elements (Parnell & Blamey, 2017; Sherwood Lollar et al., 2014; Warr et al., 2019). This slow process, fueled by the natural radioactive decay of U-Th-K, requires several million years to generate significant ^4He and H_2 amounts, as observed in the Yorke Peninsula area.

In parallel, the Precambrian basement of the peninsula hosts multiple Fe-rich units, suggesting that Fe oxidation during water-rock interactions may also contribute to the H_2 budget on the Yorke Peninsula, via the generic reaction R1. In particular, mafic metavolcanics have been reported, including the Daly Head metadolerite (Reid et al., 2022) or the Curramulka gabbronorite (Zang et al., 2007). Their occurrence echoes the extensive literature documenting natural H_2 generation during serpentinization of (ultra)mafic rocks and alteration of ferromagnesian minerals such as olivine (e.g., $Fe_{0.5}$,$Mg_{1.5}SiO_4$), via the generic reaction R2 (Klein et al., 2013; Leong et al., 2023; Marcaillou et al., 2011; McCollom et al., 2020; Neal & Stanger, 1983). Fewer studies have suggested that Fe-rich felsic rocks may also generate H_2 during water-rock interactions, based on petrographic observations (Potter et al., 2013; Salvi & Williams-Jones, 1997), experiments (Truche et al., 2021), and numerical simulations (Murray et al., 2020). Building on this, Boreham, Edwards et al. (2021) and Boreham, Sohn et al. (2021) proposed that the alteration of Fe-rich biotite (e.g., $KFe^{2+}{}_3(AlSi_3)O_{10}(OH)_2$) by circulating fluids could contribute to the subsurface H_2 generation, for instance via the generic reaction R3.

$$2FeO_{\text{mineral A}} + 1H_2O \Leftrightarrow 1Fe_2O_{3\ \text{mineral B}} + 1H_2 \quad \text{(R1)}$$

$$2Fe_{0.5},Mg_{1.5}SiO_4 + 7/3H_2O \Leftrightarrow Mg_3Si_2O_5(OH)_4 + 1/3Fe_3O_4 + 1/6H_2 \quad \text{(R2)}$$

$$1KFe^{2+}{}_3(AlSi_3)O_{10}(OH)_2 + H_2O \Leftrightarrow (K,Al,Si)\text{-silicate} + Fe_3O_4 + 1H_2 \quad \text{(R3)}$$

Utilizing petrographic and geochemical data obtained from a basement drill core sample recovered on the Yorke Peninsula, this study investigates the respective contributions of radiolysis and Fe oxidation to the H_2 fluxes reported in the region. This work emphasize the importance of combining petrography, geochemistry, and modeling to better understand H_2 systems. It also supports the growing promise of H_2 as an exploitable natural resource in stable cratonic settings.

2. Geological Settings

2.1. Basement Geology of the Yorke Peninsula

The Yorke Peninsula is located along the southeastern margin of the Gawler Craton. Like much of the craton, most of the peninsula is unconformably overlain by Phanerozoic sediments, mainly Cambrian in age, except for limited coastal exposures of the basement (Reid et al., 2008). The crystalline basement is interpreted as a highly faulted assemblage, predominantly oriented ~120°N (Figure 1). To the east, the peninsula is bounded by the Gulf of St Vincent, a localized foreland basin associated with the early Paleozoic Delamerian Orogen (Flöttman et al., 1997). The Donington Suite orthogneiss constitutes the southwesternmost part of the peninsula while the remainder corresponds to synorogenic intrusions previously assigned to the Lincoln Complex. In the central and northern regions, the poorly outcropping basement is inferred to consist of metasedimentary and metavolcanic sequences of the Wallaroo Group, mainly the Wandereah and Weetulta Formations. All terranes are crosscut by later magmatic intrusions, predominantly belonging to the Hiltaba Suite, with numerous suspected plutons identified across the peninsula and throughout southern Australia. Where exposed, the Hiltaba Suite exhibits diverse compositions ranging from adamellite and granodiorite to the well-documented gabbronorite of the Curramulka pluton (Zang et al., 2007). Notably, a recent petrographic study of Hiltaba granites from the Olympic Dam province, approximately 500 km north of the Yorke Peninsula, identified H_2-bearing fluid inclusions (Bourdet et al., 2023).

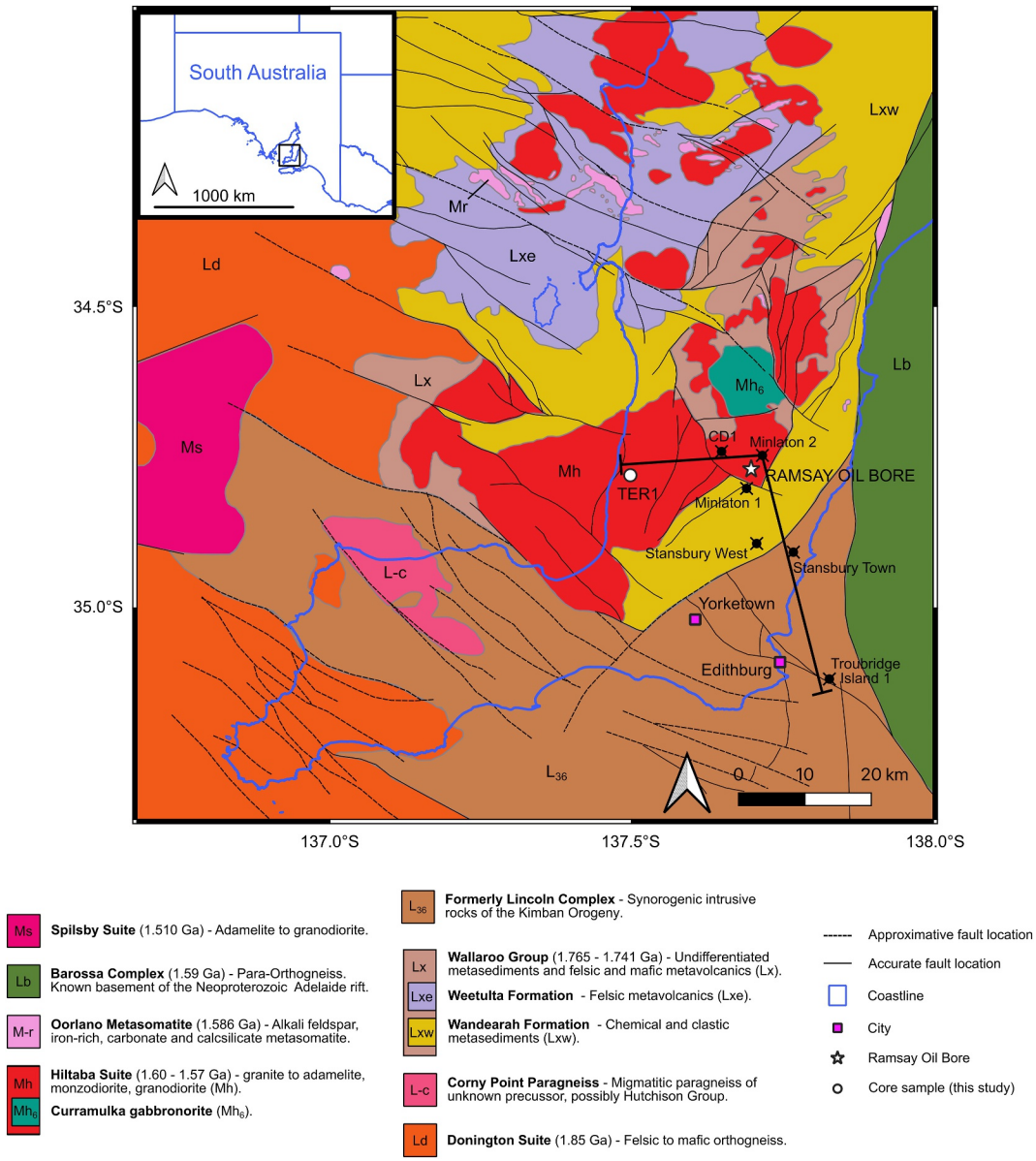

Figure 1. Basement geology of the southernmost part of the Yorke Peninsula. Modified after the Maitland SI5312 geological map of the Department for Energy and Mining SA. The black plain line represents the cross section presented in the discussion (see Section 5.5, Figure 9).

2.2. Sedimentary Cover Intersected by the Ramsay Oil Bore and TER1 Wells

A century ago, the Ramsay Oil Bore was drilled within the sedimentary cover for petroleum exploration, reaching a total depth of 548 m. Significant H_2 concentrations were detected in bubbling mud recovered from various depths, corresponding to the Cambrian Parara Limestone and Kulpara Formation (Moretti et al., 2021; Ward, 1933; Whitcombe et al., 2024). The Parara Limestone is interpreted to have been deposited in a mid to outer shelf to ramp-slope environment. It is described as a dark and nodular limestone containing clasts of peloidal wackestone within a dolomitic matrix. The underlying Kulpara Formation is generally divided into two units: a lower dolomite member carrying stromatolitic and oolitic horizons and an upper limestone member where thick beds and bioclastic packstone occur (see Castle-Jones et al. (2025), and references therein). Although the Ramsay Oil Bore did not penetrate the basement, recent geological interpretations suggest that the intrusive Hiltaba Suite constitutes the crystalline basement beneath these Paleozoic sequences (Boreham, Edwards et al., 2021;

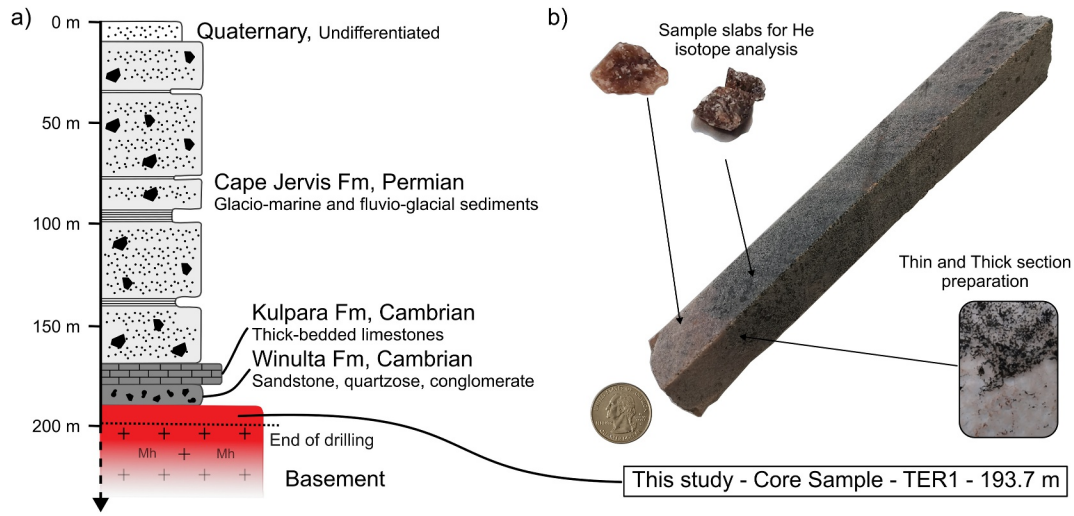

Figure 2. (a) Synthetic stratigraphy of the TER1 drillhole. Gray colors correspond to Cambrian-aged formations. Additional information on the TER1 drillhole can be found on the SARIG website, using the drillhole No 180584. (b) Photo of the sample studied. A representative photo of the thin and thick sections prepared for petrographic inspection is also provided, along with representative rock fragments used to perform quantitative analyses (e.g., helium isotope concentrations, see Section 3).

Boreham, Sohn, et al., 2021; Zang et al., 2007). Regionally, only a few boreholes have historically reached the basement, as most were drilled to assess water and hydrocarbon resources. However, the TER1 borehole (No. 180584 on the SARIG website), drilled in 2000 approximately 20 km west of the Ramsay Oil Bore, successfully intersected 9 m of the basement rock. It is interpreted as part of the Hiltaba Suite according to the latest interpretations of the regional basement geology (Figure 1). Beneath a thin Quaternary sediment veneer, the TER1 borehole penetrated the Permian Cape Jervis Formation. It is composed of five different units, all of which contain diamictites and/or glaciomarine clays that record diverse depositional environments during glaciation (Normington et al., 2018). The Cambrian Kulpara and Winulta Formations were then intersected (Figure 2a), the latter being characterized in the Yorke Peninsula by arkosic sandstones where fossil occurrences are rare (Gravestock & Shergold, 2000). Ultimately, the basement was reached at a depth of 190 m, and the drilling was terminated at a total depth of 199 m.

The sample studied in this work was collected from a TER1 drill core at a depth of 193.7 m. It consists of submillimetric felsic and mafic minerals, organized into pale-dominated or dark-dominated millimeter- to centimeter-scale bands, suggesting either foliation or crystallization processes during cooling (Figure 2b). Preliminary visual modal estimates indicate ~70–80 vol% dark-dominated bands and ~20–30 vol% pale-dominated bands. The felsic fraction includes translucent quartz, whitish plagioclase, and pinkish orthoclase, whereas the exact nature of the mafic minerals remains to be determined before this study started. No macroscopic alteration markers (e.g., pervasive veins) are observed at this scale, and the sample appears highly cohesive.

3. Analytical Tools

3.1. Bulk Rock Chemistry and Mineralogy

Inductively Coupled Plasma–Atomic Emission Spectroscopy (ICP-AES) was used to quantify major element concentrations in the bulk sample, including Fe expressed as $Fe_2O_{3\ total}$. Analyses were performed on a powder prepared from a single rock fragment representative of the entire sample, obtained by cutting across its full length. A Horiba Jobin Yvon Ultima 2 spectrometer (SEDISOR, Plouzané) was used following a protocol adapted from Cotten et al. (1995). Measurement precision is typically better than 4% for Fe_2O_3 concentrations above 1 wt%, based on international standard calibrations (BHVO-2, BCR-2, GS-N, JSD-3). In parallel, FeO titration was performed (SEDISOR, Plouzané) to determine the $Fe^{3+}/\sum Fe_{bulk}$ ratio in the sample, using the methodology detailed in Geymond et al. (2025). Briefly, $KMnO_4$ was used as the oxidizing agent following sample dissolution in HF + H_2SO_4. The protocol was validated using the same standards of known FeO concentrations. Titrations

were performed in triplicate to ensure reproducibility, yielding an overall uncertainty of ∼2% on the estimated $Fe^{3+}/\sum Fe_{bulk}$ ratio. Finally, trace element concentrations were determined by Inductively Coupled Plasma–Mass Spectrometry (ICP-MS) with a Thermo X-Series spectrometer (SEDISOR, Plouzané). GS-N international standards were used as external controls, ensuring measurement precision better than 10%.

X-ray diffraction (XRD) analyses were conducted on the same representative rock fragment to characterize the bulk rock mineralogy. A Malvern-Panalytical Empyrean diffractometer was used, equipped with a copper tube (CuKα = 1.541874 Å) and a Malvern-Panalytical multi-channel PIXcel detector (UPC, Paris). Measurements were performed over an angular range of 5°–80°, with a step size of 0.007° and a counting time of 80 s per step, corresponding to a total acquisition time of ∼1 hr. Diffractograms were interpreted through peak fitting and Rietveld refinement using the Malvern-Panalytical HighScore Plus software. Optical microscopy was subsequently employed to refine the XRD interpretations and offer a more detailed view of the mineral paragenesis. Observations were conducted on thin-sections using a Zeiss Axio microscope under both cross- and plane-polarized lights in transmission and reflection modes (IPGP, UPC, Paris).

3.2. Fluid Inclusions and Bulk Sample Gas Concentrations

Raman microspectrometry analyses were conducted on a 100 µm-thick section representative of the sample, covering both the felsic- and mafic-dominated portions (Figure 2b). Fluid inclusion compositions were investigated with a particular focus on H_2 detection. Measurements were performed using a Horiba LabRam HR Evolution spectrometer equipped with a 532 nm single-frequency 100 mW diode laser, delivering 12 mW at the focal point through a 100× objective (CSIRO Energy, Kensington). Gas detection was optimized using a grating setting of 1,800 Lines/mm. The signal was recorded with a 1,024 × 256 pixel Peltier-cooled CCD Synapse detector, sensitive in the 300–1,050 nm range. The 4,156 cm^{-1} Raman peak of H_2 was calibrated across densities ranging from 1 to 300 bar using pure H_2 calibration gas (Coregas) in a high-pressure optical cell (Chen & Chou, 2022; Chou et al., 2005; L. Li et al., 2018) and a reference calibration xenon lamp, as described in Bourdet et al. (2023).

Additionally, the composition of gases trapped within the bulk rock sample was analyzed by preparing a 56.58 g slab of the drill core sample, cut across its full length to ensure analytical representativeness. The slab was crushed in a modified ring-mill crusher under an argon atmosphere. The released gases, corresponding to the fluid inclusion fraction, were collected and analyzed using an Agilent gas chromatograph (CSIRO Energy, Kensington). The detection and quantification was optimized for H_2, CH_4, C_2H_6, N_2, and CO_2. To ensure analytical accuracy, blank tests were conducted prior to sample analysis by crushing the baked sand powder to assess potential H_2 generation artifacts. The absolute H_2 concentration measured in the drill core slab was then corrected for blank levels and normalized to mol/g of rock. In parallel, helium isotope (^3He and ^4He) bulk concentrations were measured on separate bulk rock aliquots that were fused in vacuum (CRPG, Univ. de Lorraine, Nancy), following the protocol described in Doll et al. (2024). This high-precision methodology is designed to operate on small cohesive samples (i.e., not ground prior to analysis in order to prevent He loss), which precluded analysis of our entire sample in a single measurement. For this reason, two cm-sized slabs were prepared to evaluate sample heterogeneity, comprising a 224 mg felsic-dominated sub-sample and a 227 mg mafic-dominated sub-sample (Figure 2b). These slabs were melted at 1,500°C under ultra-high vacuum for 15 min to release trapped gases from both the crystal lattice and fluid inclusions. The gases were purified by physisorption onto various hot and cold traps to isolate He from other gas species. Helium was subsequently condensed using a 12 K cryogenic trap and released at 75 K for isotope measurement in static mode using a GV Instruments Helix Split Flight Tube multi-collector noble gas mass spectrometer (CRPG, Univ. de Lorraine, Nancy). Background levels were monitored throughout the analytical period by daily quantification of ^3He and ^4He blanks, yielding 1.7×10^{-19} mol and 1.1×10^{-14} mol, respectively.

3.3. Mineral Texture and Chemistry

Scanning electron microscopy (SEM) was performed to further constrain the sample's paragenesis and qualitatively assess the chemistry of Fe-bearing minerals. A Zeiss Auriga 40 SEM was used, equipped with a 1 nm resolution Field Emission Gun (FEG) and a Bruker Quantax 800 Energy Dispersive Spectroscopy (EDS) system featuring a Bruker XFlash 410-M detector (IPGP, UPC, Paris).

An electron probe microanalyzer (EPMA) was utilized to determine the chemical composition of minerals of interest, specifically biotite and chlorite. Analyses were conducted using a Cameca SX-100 (ISTeP, SU, Paris), operating at an accelerating voltage of 15 keV and a beam current of 30 nA, with a counting time of 50 ms per pixel and a spatial resolution step of 4 µm. Diopside (Ca, Mg, Si), $MnTiO_3$ (Mn, Ti), orthoclase (K, Al), Fe_2O_3 (Fe), and albite (Na) were used as internal standards for the calibration of elements in parentheses. Once the detectors were calibrated, representative point analyses were performed across the entire sample. For biotite, mineral cores were targeted to minimize potential edge-effect contamination. For chlorite, all EPMA analyses yielding $K_2O + Na_2O + CaO > 1$ wt% were discarded to exclude contamination from surrounding minerals, following the criteria established previously by Bourdelle, Parra, et al. (2013).

A location of interest was selected during the SEM observations to perform a Focused Ion Beam (FIB) section into the thin section. The FIB section was extracted using a Zeiss Auriga 40 (IPGP, UPC, Paris). To prevent ion-induced damage, the selected area was protected with a 1.2 µm-thick Pt coating prior to ion beam milling (Ga^+) on both sides of the section. The extracted FIB section, measuring approximately 10–15 µm × 5 µm, was welded onto finger-shaped TEM grids and subsequently thinned to a thickness of approximately 100 nm. Final cleaning was performed using a low-energy Ga beam at grazing incidence. Throughout the milling process, the ion beam voltage and current were carefully controlled to minimize amorphization.

The FIB section was analyzed using Scanning Transmission X-ray Microscopy (STXM) and X-ray Absorption Near-Edge Structure (XANES) spectroscopy at the HERMES STXM beamline of the SOLEIL synchrotron (Belkhou et al., 2015; Swaraj et al., 2017). The acquisition of XANES hyperspectral data cubes enabled the determination of Fe speciation from the absorption spectrum of each pixel, ultimately providing a Fe speciation map of the FIB section. XANES data were acquired from image stacks collected at energy increments of 0.1 eV across the iron absorption range (690–740 eV), with a dwell time of 1 ms per pixel to prevent irradiation damage (Wang et al., 2009). Following recent studies (Combaudon et al., 2024; Megevand et al., 2025) and adapting the methodology initially developed by Bourdelle, Benzerara, et al. (2013) and Le Guillou et al. (2015), relative $Fe^{3+}/\sum Fe$ ratios were estimated by fitting Fe^{2+} and Fe^{3+} peaks after background subtraction and calculating peak surface ratios. However, as noted by these authors, quantitative assessment of $Fe^{3+}/\sum Fe$ using STXM-XANES remains highly challenging, as the signal intensity may vary depending on the nature of the clay minerals investigated. Therefore, no such absolute quantification was conducted in this study to avoid potential misinterpretation.

The FIB section was further studied via Transmission Electron Microscopy (TEM) using a JEOL 2100F equipped with a FEG operating at an acceleration voltage of 200 kV (IMPMC, UPC, Paris). Specifically, Scanning Transmission Electron Microscopy (STEM) mode was employed to perform EDS analyses on regions of interest and to generate elemental maps, utilizing a rastering electron beam with a spot size ranging from 0.7 to 1.5 nm. Given the potential sensitivity of the FIB section to STEM analyses and the risk of beam-induced mineral alteration, the sample was examined by STXM-XANES before being analyzed in TEM-STEM mode.

4. Results

4.1. Bulk-Rock Chemistry and Paragenesis

The sample is characterized by an elevated iron concentration, with $\sum Fe$ (expressed as Fe_2O_3) reaching 5.65 wt%. A significant portion of the iron is in the ferrous state, with an $Fe^{3+}/\sum Fe_{bulk}$ ratio of 0.14. Other major elements include SiO_2 (64.86 wt%), Al_2O_3 (14.12 wt%), TiO_2 (0.55 wt%), MgO (2.39 wt%), CaO (3.51 wt%), Na_2O (3.04 wt%), and K_2O (3.38 wt%). Regarding trace elements, U and Th show concentrations of 2.57 and 20.81 ppm, respectively. The complete bulk geochemical data set is provided in Table S1.

The XRD analysis (Figure 3a) and subsequent mineral quantification indicate that the bulk sample is composed of quartz (17.3 wt%), feldspars—including orthoclase (15.1 wt%) and anorthite (42.1 wt%)—as well as amphibole (8.0 wt%), biotite (11.6 wt%), chlorite (3.1 wt%), and clinopyroxene (2.9 wt%). The latter is only weakly visible in the XRD pattern. This paragenesis was confirmed by optical microscopy observations (Figures 3b and 3c). Feldspar grains exhibit pronounced sericitization, giving them a flaky appearance. Although quartz is less abundant than feldspar, it is widely distributed throughout the sample. Observations also confirm the presence of amphibole, identifiable by its olive-green color and characteristic 120° cleavages, as well as pyroxene, which

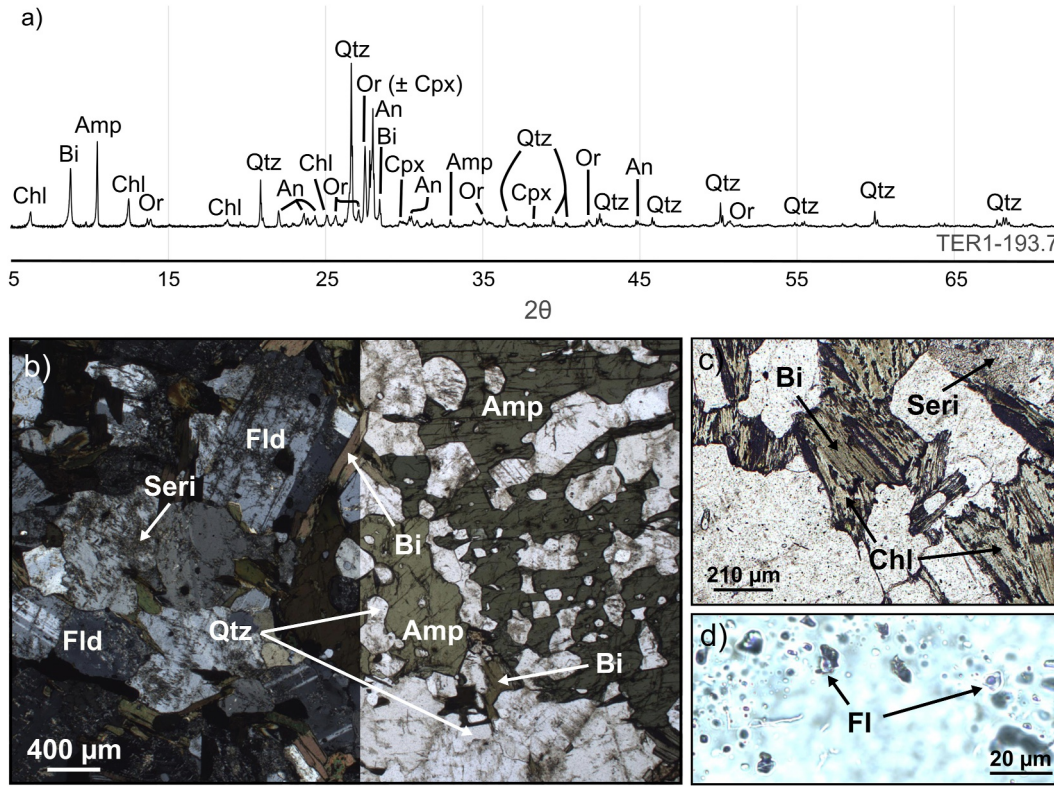

Figure 3. (a) XRD pattern and associated peak indexing. Mineral abbreviations: Amp, amphibole; An, anorthite; Bi, biotite; Chl, chlorite; Or, Orthose; Qtz, quartz. (b) Representative paragenesis of the studied sample, observed by optical microscopy under cross-polarized (LPA) and plane-polarized (LPNA) light. Clinopyroxene identified by XRD is not present in the image. (c) Close-up view of biotite undergoing pseudomorphosis into chlorite. (d) Close-up view of a cluster of gas-bearing fluid inclusions (FI) within quartz.

appears light green with distinctive 90° cleavages. Biotite is clearly visible as light brown lamellae, distinguished by its strong basal cleavage and high birefringence. The irregular rims of biotite suggest an alteration pattern consistent with the presence of chlorite, as detected by XRD.

Interestingly, local-scale observations reveal the presence of thousands of gas-bearing fluid inclusions within quartz, ranging in size from 1 to 10 µm (Figure 3d). These inclusions exhibit rounded to irregular shapes.

4.2. Fluid Inclusions and Gas Content

Among the diversity of fluid inclusions (FI) observed in the sample, we focused our investigation on those identified within the quartz matrix (the sample is quartz-vein-free). A significant proportion of the FI are distributed along planar arrays, exhibit highly irregular morphologies, and vary in size from 1 to 20 µm (Figures 4a–4c). Raman microspectrometry was performed exclusively on the largest inclusions to minimize light scattering for too small inclusions. In many of the analyzed FI, the presence of H_2 and N_2 is identified by the peak positions (i.e., Raman shift) at 4,156 cm^{-1} and 2,330 cm^{-1}, respectively (Figure 4d; Frezzotti et al., 2012). A broad spectral band corresponding to liquid H_2O is also observed, with an intensity varying as a function of inclusion size and scattering. Importantly, no Raman signals corresponding to CH_4 (2,917 cm^{-1}) or CO_2 (1,285 and 1,388 cm^{-1}) could be detected in any of the analyzed FI.

Crushing analyses provide complementary results consistent with the Raman microspectrometry data, showing the presence of N_2 and H_2 with relative concentrations of 0.17 and 0.46 $mmol/kg_{rock}$, respectively. No other gaseous species could be detected using this technique.

Finally, helium isotope measurements indicate the presence of He in both mafic-dominated and felsic-dominated sample slabs (raw data are available in Table S2. Concentrations in the mafic-dominated slab

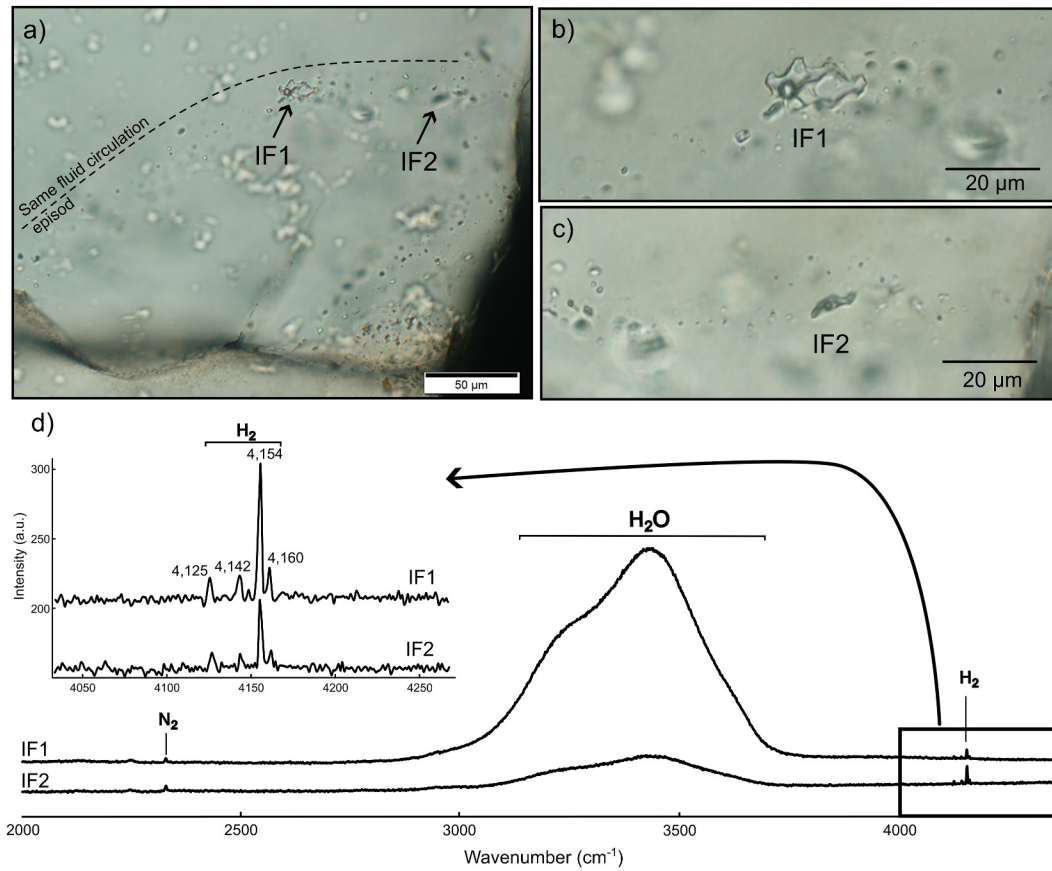

Figure 4. (a–c) Quartz-hosted fluid inclusions (FI) observed by optical microscopy on thick sections and (d) typical Raman spectra obtained after FI analyses. For one fluid trapping episode (inclusions aligned), FI are highly heterogeneous in size, allowing Raman analyses only on a few of them. The peak at 2,330 cm^{-1} and the four peaks from 4,125 to 4,160 cm^{-1} are characteristic of N_2 and H_2, respectively. Please note that the presence of CH_4 (2,917 cm^{-1}) and CO_2 (1,285, 1,388 cm^{-1}) was also investigated but was not detected. The bulge of water is observed and varies in intensity with the size of the inclusion due to scattering of Raman rays.

yielded $(8.83 \pm 0.06) \times 10^{-1}$ $\mu mol.kg^{-1}_{rock}$ (^4He) and $(6.79 \pm 0.66) \times 10^{-9}$ $\mu mol.kg^{-1}_{rock}$ (^3He), while they were $(7.03 \pm 0.05) \times 10^{-1}$ $\mu mol.kg_{rock}$ (^4He) and 2.99×10^{-10} $\mu mol.kg^{-1}_{rock}$ (^3He) for the felsic-dominated slab. The corresponding ratios of $^3He/^4He$ are 0.0056 ± 0.0005 R/Ra (mafic-dominated slab) and 0.0003 R/Ra (felsic-dominated slab), where Ra refers to the $^3He/^4He$ atmospheric ratio ($Ra = 1.39 \times 10^{-6}$; Boucher et al., 2018).

4.3. Fe^{2+}-Bearing Mineral Textures and Chemistry

According to bulk-sample mineral and chemical characterization, Fe occurs mostly as Fe^{2+}, mainly carried by amphibole and biotite. A deeper investigation of their textures and chemistry is relevant to quantify the contribution of Fe oxidation to H_2 generation. This was performed using high-resolution observation and quantifications, using SEM, EPMA STXM and TEM.

4.3.1. Amphibole and Clinopyroxene

SEM images show well-preserved rims on amphibole grains, indicating that the minerals did not undergo significant alteration (Figures 5a and 5b). Amphibole is surrounded by quartz and feldspar, with the latter being easily identified by its characteristic glittery sericite texture. Primary euhedral titanite is also observed. A few fractures are observed, crosscutting both amphibole and adjacent minerals. These fractures are filled by calcite, forming discrete veins. No Fe-rich secondary phases are visible within the veins, and vein walls in contact with amphibole are sharp, lacking any visible chemical gradients (e.g., in Fe) or alteration textures. These features

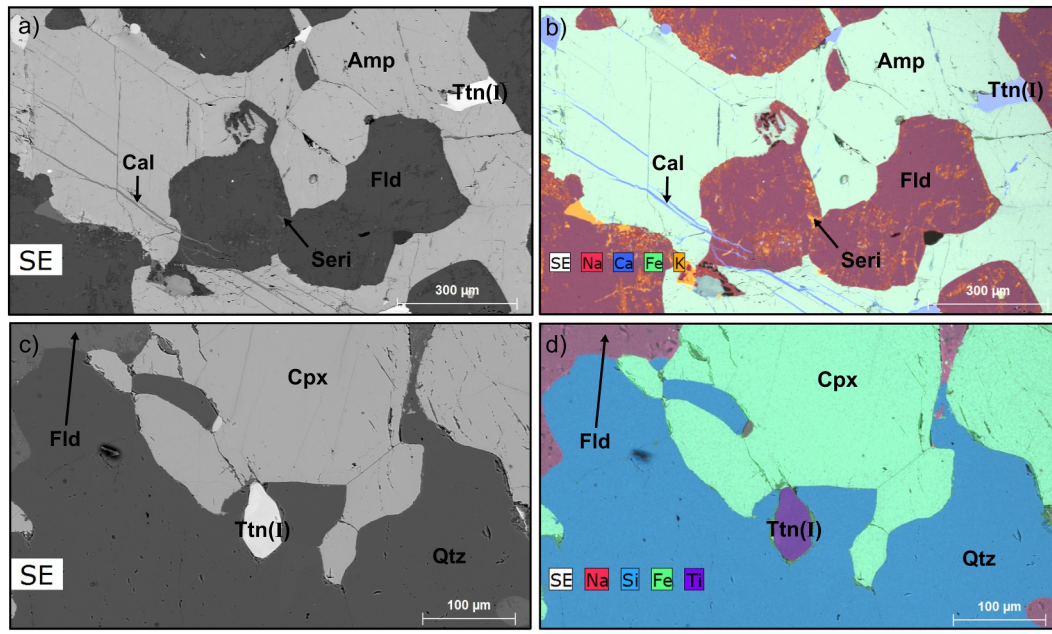

Figure 5. (a) Scanning electron microscopy backscattered electron image and (b) chemical map of an amphibole. The mineral boundaries are sharp and no alteration pattern is observed. Calcite vein crosscuts both amphibole and feldspar but does not seem to be related to Fe solubilization. Same conclusions apply for clinopyroxene, as visible in (c) Backscattered electron image and (d) chemical map of a clinopyroxene. Primary titanite is evidenced thanks to Ca and Ti chemical maps (as well as Si map, not provided here). Mineral abbreviations: Qtz, quartz; Fld, feldspar; Amp, amphibole; Seri, sericite; Cal, calcite; Ttn(I), primary titanite.

suggest that amphibole remained stable during the fluid circulation event responsible for vein formation. Similar observations were made for clinopyroxene (Figures 5c and 5d). Grain boundaries are sharp and show no evidence of dissolution textures that suggest iron mobilization. As no textural or mineralogical indicators of iron oxidation could be observed in either amphibole or clinopyroxene, detailed chemical analyses of these phases are not discussed further.

4.3.2. Biotite and Chlorite

SEM observations and potassium mapping validate the presence of biotite along with alteration textures corresponding to chlorite (see Figure 3c), as K is a preponderant component of biotite and is absent in chlorite (Figures 6a and 6b). Representative EPMA point analyses performed on biotite and chlorite are presented in Tables 1 and 2, respectively. Several of the analyzed spots are visible in Figure 6a. These raw results are further discussed in Section 5.1.2. Along with chlorite, secondary titanite and sparse Fe-oxides were detected, labeled Ttn (II) and Fe-ox(II), respectively. Ttn(II) and Fe-ox(II) are distinguished from titanite and Fe-oxide of primary origin by their morphologies. Primary minerals appear euhedral and hundreds of micrometers in size (see Figure 5 for an example of primary titanite), while secondary titanite and Fe-oxide are micrometric to sub-micrometric in size with irregular shapes (Figure 6b). More specifically, Fe-ox(II) is observed infilling sub-micrometric cracks following former biotite cleavages. Due to its very small size, the nature of Fe-ox(II), magnetite or hematite could not be constrained unambiguously. The extracted FIB section crosscuts all phases of interest, as observed with elemental mapping performed during TEM sessions (Figure 6c). Fe-ox(II) and Ttn(II) are easily distinguished by Ti and Fe mapping, and the variability in potassium concentrations within the surrounding silicate minerals highlights interlayered sheets of biotite and chlorite at the micrometric scale (K mapping). The STXM-XANES transect performed on the FIB section allows for the qualitative investigation of $Fe^{3+}/\Sigma Fe$ in chlorite and biotite (Figure 6d). Apart from Fe-ox(II), which could not be analyzed via STXM due to its too high Fe content, the results highlight heterogeneities in Fe speciation at the sub-micrometric scale. These variations correspond to chloritization and biotite replacement, where the more oxidized sheets primarily correspond to biotite and the less oxidized sheets primarily correspond to chlorite. This is supported by the TEM chemical mapping of potassium (Figure 6c), allowing biotite (K-rich) and chlorite (K-poor) to be located along the transect. Any other

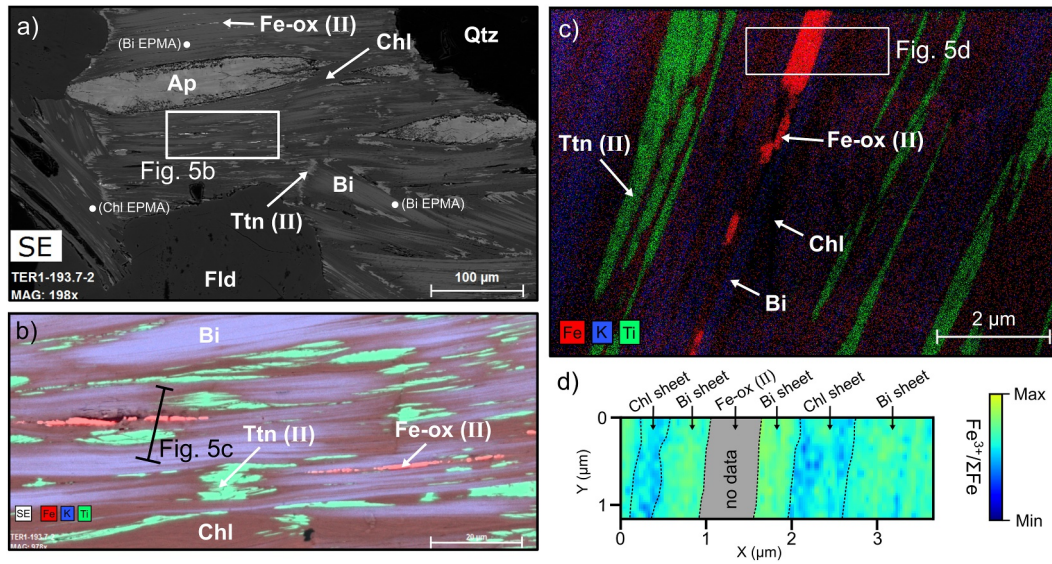

Figure 6. (a, b) Scanning electron microscopy backscattered electron image and corresponding chemical map showing a biotite grain undergoing alteration into chlorite, titanite and Fe-oxide. Mineral abbreviations: Fld, feldspar; Bi, biotite; Chl, chlorite; Ap, apatite; Ttn(II), secondary titanite; Fe-ox(II), secondary iron oxide. Representative spots selected for EPMA analyses are indicated in (a). (c) TEM chemical mapping of the Focused Ion Beam (FIB) section extracted within an altered biotite grain, highlighting secondary titanite (green) and Fe-oxide precipitates (red). Potassium mapping (blue) allows to distinguish interlayered biotite (K-rich) and chlorite (K-poor) sheets at the micrometer scale. The exact position of the FIB section is shown in (b). (d) STXM-XANES transect performed in the FIB section qualitatively showing $Fe^{3+}/\Sigma Fe$ variability. Higher $Fe^{3+}/\Sigma Fe$ (bright green) is interpreted as unaltered biotite, whereas lower $Fe^{3+}/\Sigma Fe$ (blue color) is interpreted as chlorite. The gray color represents the area with "no data" due to complete X-ray absorption by Fe-rich, dense, or overly thick minerals, preventing transmission through the FIB section. In this case, these areas correspond to Fe-ox(II).

intermediate $Fe^{3+}/\Sigma Fe$ presumably corresponds to a close mixing between the two "end-members," chlorite and biotite sheets, at the sub-micrometric scale and below the spatial resolution threshold. Iron speciation in biotite and chlorite is further discussed in Section 5.1.2.

5. Discussions

By highlighting the presence of H_2-bearing fluid inclusions, our petrographic study supports the recent hypothesis that Hiltaba Suite granites generated H_2 within the basement of the Yorke Peninsula (Boreham, Edwards et al., 2021; Boreham, Sohn, et al., 2021). The mechanisms responsible for such H_2 occurrence warrant further investigation and are discussed herein. We specifically focus on radiolysis and Fe oxidation, which are the main H_2 production pathways proposed in the literature. It is important to note that this discussion relies on a new petrographic data set acquired from a single sample. As such, any proposed interpretation or extrapolation to the regional scale must be viewed with caution.

5.1. Constraints on a Possible H_2 Contribution From Fe Oxidation

5.1.1. The Promise of a Fe^{2+}-Rich Lithology

The studied sample is Fe^{2+}-rich at the bulk scale (5.65 wt% ΣFe, $Fe^{3+}/\Sigma Fe_{bulk} = 0.14$). This suggests that Fe oxidation may play a role in H_2 generation if the sample undergoes alteration (see Reaction R1). Ferrous iron is mainly hosted by primary silicate minerals. Some of them (i.e., clinopyroxene, amphibole) have been identified as H_2 sources during anoxic water-rock interactions (e.g., Marcaillou et al., 2011; Truche et al., 2021). Interestingly, clinopyroxene and amphibole do not show any textural markers of alteration that could suggest Fe^{2+} mobilization and subsequent oxidation (Figure 5). This observation rules out any significant H_2 production from those minerals. Conversely, biotite appears chloritized, with secondary Fe-oxide present in cracks and cleavage planes. This suggests the mobilization and oxidation of Fe during chloritization, raising the potential for H_2 generation associated with the destabilization of biotite. This observation supports an earlier work proposing that the H_2 measured in the Yorke Peninsula may originate from the alteration of Fe-rich biotite, a major constituent of the

Table 1
EPMA Raw Data (wt%) and Formula Units of Biotite Calculated Following the Methodology of X. Li et al. (2020)

Analysis	1	2	3	4	5	6	7	8	9	10	11	12	Mean
SiO_2	35.37	34.63	35.21	34.71	35.53	35.15	34.74	35.06	35.07	35.42	34.01	34.41	34.94
TiO_2	2.99	2.88	2.92	2.83	2.82	2.65	2.84	3.30	3.29	2.91	3.03	2.76	2.94
Al_2O_3	14.17	14.70	13.93	14.10	14.24	14.19	13.66	13.69	13.65	13.82	14.00	14.28	14.03
FeO_t	18.14	17.84	17.12	17.87	17.87	17.57	17.38	17.34	17.67	17.48	17.66	17.92	17.65
MnO	0.27	0.21	0.22	0.20	0.24	0.25	0.27	0.23	0.27	0.20	0.23	0.24	0.24
MgO	13.14	13.12	12.89	12.77	12.73	12.79	12.27	12.18	12.13	12.72	12.67	12.69	12.68
CaO	0.04	0.19	0.03	0.02	0.00	0.01	0.03	0.05	0.13	0.08	0.05	0.09	0.06
Na_2O	0.08	0.09	0.05	0.07	0.10	0.11	0.09	0.07	0.08	0.13	0.10	0.08	0.09
K_2O	8.73	7.36	9.22	8.91	8.81	9.20	9.51	9.16	9.19	8.36	8.72	8.12	8.77
Total	92.92	91.03	91.59	91.46	92.34	91.92	90.79	91.09	91.49	91.12	90.47	90.58	91.40
Si	2.76	2.72	2.79	2.75	2.78	2.77	2.79	2.80	2.80	2.80	2.74	2.74	2.77
^{IV}Al	1.05	1.10	0.96	1.02	1.02	1.03	0.97	0.98	0.96	0.96	1.04	1.02	1.01
^{VI}Al	0.26	0.27	0.34	0.30	0.30	0.29	0.32	0.31	0.32	0.32	0.29	0.32	0.30
$^{IV}Fe^{3+}$	0.19	0.18	0.25	0.22	0.20	0.20	0.24	0.22	0.24	0.24	0.23	0.24	0.22
$^{VI}Fe^{3+}$	0.10	0.18	0.05	0.08	0.08	0.06	0.01	0.04	0.04	0.10	0.08	0.12	0.08
Fe^{2+}	0.89	0.81	0.84	0.88	0.89	0.90	0.92	0.90	0.90	0.82	0.88	0.83	0.87
Mg	1.54	1.55	1.57	1.54	1.50	1.52	1.52	1.50	1.49	1.54	1.56	1.55	1.53
Ti	0.18	0.17	0.18	0.17	0.17	0.16	0.18	0.20	0.20	0.18	0.18	0.17	0.18
K	0.88	0.78	0.91	0.90	0.89	0.92	0.95	0.92	0.92	0.84	0.89	0.83	0.88
Σ vacancy	0.16	0.25	0.12	0.13	0.18	0.14	0.11	0.14	0.13	0.21	0.12	0.18	0.15
OH^-	1.60	1.62	1.65	1.67	1.65	1.69	1.67	1.61	1.61	1.62	1.65	1.65	1.64
O^{2-}	0.33	0.38	0.26	0.32	0.34	0.31	0.32	0.38	0.37	0.37	0.34	0.33	0.34
$Fe^{3+}/\Sigma Fe$	0.25	0.31	0.26	0.26	0.24	0.22	0.22	0.22	0.24	0.29	0.26	0.30	0.26

Note. The spreadsheet used for the calculations was developed by Gündüz and Asan (2023).

granitic basement beneath the Ramsay Oil Bore (Boreham, Edwards et al., 2021; Boreham, Sohn, et al., 2021). It also aligns with recent numerical modeling evaluating H_2 generation during the alteration of biotite-rich granite by brine under open-system conditions at temperatures of 130–200°C (Murray et al., 2020). This study predicted biotite dissolution coupled with the precipitation of secondary magnetite or hematite—consistent with our observations (Figure 6)—along with H_2 generation. At first glance, such numerical simulations support the hypothesis that biotite chloritization within the Hiltaba granite could lead to H_2 generation. The apparent agreement between literature-based assumptions and our petrographic observations highlights the need to better constrain the biotite chloritization reaction in our sample.

5.1.2. Composition and Fe Redox of Biotite and Chlorite

A precise determination of the composition and Fe redox state of biotite and chlorite is required to evaluate whether H_2 in the sample originates from biotite chloritization. Concerning Fe redox, uncertainties prevent accurate quantification from the STXM-XANES data due to the intimate mixing of minerals at the sub-micrometric scale (Figure 6). Consequently, no attempt was made to perform absolute $Fe^{3+}/\Sigma Fe$ estimates from STXM-XANES, although data clearly indicate that the Fe is more reduced in chlorite than in biotite (Figure 6d).

Concerning the composition and Fe redox state of biotite, formula units were reconstructed using EPMA raw data. The low oxide totals (mean = 91.40 wt%, Table 1) relative to standard biotite (typically <95 wt%) can be interpreted as resulting from partial alteration, which lowers oxide totals. This is consistent with our TEM observations, which highlighted interlayered chlorite-biotite at the sub-micrometric scale (Figure 6). The machine learning- and PCR-based methodology developed by X. Li et al. (2020) was employed, enabling the direct

Table 2
EPMA Raw Data (wt%) and Formula Units of Chlorite Calculated on the Basis of 14 Oxygens

Analysis	13	14	15	16	17	18	19	20	21	22	23	Mean
SiO_2	27.99	27.24	26.93	27.41	27.56	28.09	27.62	27.22	27.07	28.77	28.18	27.64
TiO_2	0.08	0.06	0.10	0.05	0.15	0.13	0.14	0.08	0.03	0.15	0.03	0.09
Al_2O_3	16.27	16.80	17.03	17.00	16.05	15.63	16.78	15.75	16.22	16.22	16.72	16.41
FeOt	21.91	20.74	21.15	21.05	21.06	22.03	20.15	22.16	22.10	18.95	19.67	21.00
MnO	0.37	0.34	0.43	0.48	0.38	0.49	0.53	0.41	0.37	0.30	0.42	0.41
MgO	17.94	18.46	18.38	18.64	18.49	17.68	19.08	17.74	17.61	20.09	20.39	18.59
CaO	0.09	0.03	0.10	0.08	0.09	0.05	0.07	0.09	0.04	0.07	0.02	0.07
Na_2O	0.03	0.00	0.01	0.00	0.00	0.01	0.00	0.01	0.02	0.01	0.02	0.01
K_2O	0.03	0.02	0.03	0.02	0.24	0.15	0.15	0.00	0.03	0.23	0.05	0.09
Total	84.70	83.68	84.17	84.73	84.02	84.25	84.53	83.47	83.49	84.80	85.50	84.30
Si	3.02	2.95	2.92	2.95	3.00	3.06	2.97	2.99	2.97	3.05	2.97	2.99
^{IV}Al	0.98	1.05	1.08	1.05	1.00	0.94	1.03	1.01	1.03	0.95	1.03	1.01
^{VI}Al	1.09	1.10	1.10	1.10	1.06	1.06	1.10	1.04	1.07	1.08	1.05	1.08
Mg	2.84	2.89	2.91	2.87	2.89	2.89	2.76	2.95	2.81	2.78	3.08	2.90
Fe^{2+}	1.65	1.82	1.86	1.85	1.83	1.85	1.93	1.75	1.97	1.96	1.63	1.82
Σ Vacancy	0.05	0.03	0.01	0.02	0.03	0.06	0.03	0.02	0.02	0.06	0.01	0.03
OH	8.00	8.00	8.00	8.00	8.00	8.00	8.00	8.00	8.00	8.00	8.00	8.00
$Fe^{3+}/\Sigma Fe$[a]	0.00	0.00	0.00	0.00	0.00	0.00	0.00	0.00	0.00	0.00	0.00	0.00
R^{2+}[b]	4.86	4.87	4.89	4.88	4.92	4.88	4.87	4.95	4.91	4.86	4.94	4.89

Note. The spreadsheet used for calculations is available in Table S3. [a]$Fe^{3+}/\Sigma Fe$ is set to 0 to calculate the formula units from EPMA raw data ($\Sigma Fe = Fe^{2+}$) to calculate a geothermometer and equilibrate a reaction equation. [b]$R^{2+} = Mg^{2+} + Fe^{2+}$ and is used to calculate a geothermometer (see Section 5).

determination of biotite formula units and $Fe^{3+}/\Sigma Fe_{biotite}$ with greater accuracy than previously proposed methods. This methodology was specifically selected because it provides $Fe^{3+}/\Sigma Fe_{biotite}$ values representative of initial biotite, even when the mineral has undergone post-crystallization alteration. Iron appears partially oxidized, with a mean calculated $Fe^{3+}/\Sigma Fe_{biotite}$ of 0.26 (Table 1). The uncertainty in the $Fe^{3+}/\Sigma Fe$ ratio is estimated at ±10%, given that the total Fe content in biotite reaches 18 wt% FeO (see X. Li et al. (2020) for a detailed discussion of the associated uncertainty). Overall, the simplified composition of biotite, excluding trace elements such as Mn, Ca, and Na, is mostly homogeneous across the 12 analyses (Table 1). The mean calculated formula unit is as follows, where □ represents vacancies within the mineral lattice:

$$(K_{0.88}, \square_{0.12})\left(Mg_{1.53}, Ti_{0.18}, Fe^{3+}{}_{0.08}, Fe^{2+}{}_{0.87}, Al_{0.30}, \square_{0.04}\right)\left(Si_{2.77}, Al_{1.01}, Fe^{3+}{}_{0.22}\right)O_{10}(OH, O^{-})_2.$$

Similar to biotite, the formula units of chlorite were reconstructed using the EPMA raw data on the basis of 14 oxygens (Table 2). For the sake of clarity, trace elements such as K, Na, and Ca were not considered when calculating the simplified formula units. This approximation is justified as the use of a chlorite-based geothermometer (presented in Section 5.3.1) requires a pure end-member composition (see for instance Inoue et al. (2018)). Concerning Fe redox, there is currently no established consensus on a reliable methodology for determining $Fe^{3+}/\Sigma Fe_{chlorite}$ directly from EPMA data. Therefore, all iron was assumed to be Fe^{2+} in the calculations. This approximation is supported by STXM-XANES, which show that $Fe^{3+}/\Sigma Fe_{chlorite} < Fe^{3+}/\Sigma Fe_{biotite}$, while $Fe^{3+}/\Sigma Fe_{biotite} = 0.26$ according to our biotite formula unit reconstruction. In addition, this approximation is convenient since reaction balancing (presented in Section 5.1.3) and geothermometer calculations (Section 5.3.1) require the assumption that $\Sigma Fe = Fe^{2+}$. Chlorite appears heterogenous in composition across the 11 analyses (Table 2). The simplified mean calculated chlorite composition, where □ represents vacancies within the mineral lattice, is given as follows:

$$\left(Mg_{2.99}, Fe^{2+}{}_{1.90}, Al_{1.08}, \square_{0.03}\right)\left(Si_{2.99}, Al_{1.01}\right)O_{10}(OH)_8$$

Overall, EPMA-derived formula unit calculations for biotite and chlorite, as well as the STXM-XANES transect performed at the biotite-chlorite interface, indicate that Fe is more oxidized in primary biotite than in secondary chlorite (Figure 6d). This casts doubt on the possibility that this mineral transformation sources H_2. However, a precise mass balance calculation, accounting for the Fe partitioning between Fe-ox(II) and chlorite during biotite alteration, is still required to conclude on a possible Fe-driven H_2 generation during chloritization.

5.1.3. H_2 Generation Estimate From Reaction Balancing of Fe-Biotite Alteration

To further test the hypothesis of a Fe-driven H_2 generation during chloritization, a chemical reaction was tentatively balanced using the methodology developed by Godard (2010). This methodology must be applied with caution, as it is a purely mathematics-based protocol for reaction balancing that does not account for the physicochemical feasibility (e.g., thermodynamics) of the resulting reaction. In addition, it assumes a closed and conservative reactive system, whereas natural systems are most likely open, and most mobile elements may thus be lost from the system. Despite these limitations, the methodology provides a valuable first-order framework for exploring mineral transformations. Ten phases were considered as input data:

1, 2. **Chlorite (Chl) and biotite (Bi),** using formula units calculated in Section 5.1.2. For the purpose of this reaction balancing, all iron was treated as a single, undifferentiated component (ΣFe), regardless of its oxidation state, to maintain a conservative system. The redox state of Fe is addressed separately in the following discussion;

3, 4. **Ideal titanite (Ttn(II), $CaTiSiO_5$) and Fe oxide (Fe-ox(II), Fe_3O_4),** both observed as products of the alteration reaction. It should be noted that the precise identity of the Fe-ox(II) precipitate remains uncertain; consequently, the formula unit for hematite (Fe_2O_3) could have been used instead of magnetite (Fe_3O_4) to balance the reaction;

5, 6, 7. **Ideal quartz (Qtz, SiO_2), anorthite (An, $CaAl_2Si_2O_8$) and sericite (Seri, $KAl_3Si_3O_{10}(OH)_2$),** which all occur in the matrix surrounding the chloritized biotite. The formula unit for muscovite ($KAl_3Si_3O_{10}(OH)_2$) was used to balance the reaction, as it is the dominant white mica endmember in the sericite;

8, 9, 10. **Water (H_2O) and highly mobile cations (H^+ and K^+).** By constraining the system with the dissolution of 1 mol of biotite, the remaining nine phases are defined by nine independent components (Si, Al, ΣFe, Mg, O, H, K, Ti, and Ca), thus forming a fully determined system (i.e., a Cramer's system; see Figure S1 in Supporting Information S1). This allows for a single balanced reaction R4 to be calculated:

$$1Bi + 0.18An + 1.38H_2O + 0.10H^+ \rightarrow 0.51Chl + 0.07Fe - ox(II) + 0.18Ttn(II) + 0.20Seri + 0.82Qtz + 0.68K^+ \quad (R4)$$

According to this reaction, biotite destabilization leads to the precipitation of Fe-ox(II) and chlorite, which sequester the released ferrous iron. The limited amount of magnetite predicted by the reaction balancing is consistent with SEM observations, where Fe-ox(II) appears only sporadically. During biotite dissolution, Ti is also released and subsequently incorporated into Ttn(II), as observed in the sample. Ttn(II) growth requires Ca^{2+}, supplied by anorthite dissolution, which also furnishes the required substrate for sericite precipitation. The newly formed sericite incorporates part of the K^+ released during biotite dissolution, while the remaining fraction is likely mobilized and removed from the system by circulating fluids. Finally, H^+ is considered as a reactant in this reaction. It is worth noting that our proposed reaction closely resembles those in the literature describing the chloritization process, which is known to induce Fe mobilization and Fe-ox(II) precipitation, namely magnetite (Eggleton & Banfield, 1985; Parry & Downey, 1982). In these earlier studies, H^+ is also considered as a reactant. However, in all cases, ferrous iron is treated as a non-redox component during reaction balancing (i.e., fixed ΣFe in this study, and fixed Fe^{2+} and Fe^{3+} in previous works). As a result, the redox dynamics of Fe, and consequently the potential for H_2 generation or consumption, cannot be directly assessed through these equations. To address this caveat, another reaction R5 was balanced by substituting H^+ by H_2 as a reactant:

$$1Bi + 0.18An + 1.38H_2O + 0.05H_2 \rightarrow 0.51Chl + 0.07Fe - ox(II) + 0.18Ttn(II) + 0.20Seri + 0.82Qtz + 0.68K^+ \quad (R5)$$

This new reaction introduces the redox state of the fluid as an active factor, with H_2 now explicitly participating in the reaction. As Fe is the only other redox-sensitive element considered, the consumption of 0.05 mol of H_2 (i.e., its oxidation) necessarily implies the simultaneous reduction of 0.10 mol of Fe^{3+} (see reaction R1). Therefore, considering that Fe from biotite ($\Sigma Fe_{biotite} = 0.17$, $Fe^{3+}/\Sigma Fe_{biotite} = 0.26$, see Table 1) is partitioned between Fe-ox(II) (i.e., magnetite Fe_3O_4, $Fe^{3+}/\Sigma Fe_{magnetite} = 0.67$) and chlorite during the reaction, the reduction of 0.10 mol of Fe corresponds to a theoretical $Fe^{3+}/\Sigma Fe_{chlorite} = 0.08$ (refer to Text S1 in Supporting Information S1 for the detailed calculations). As no quantitative in situ data currently confirm this $Fe^{3+}/\Sigma Fe_{chlorite} = 0.08$ value, it remains speculative. Nevertheless, it is qualitatively supported by the STXM-XANES transect, which shows a higher $Fe^{3+}/\Sigma Fe$ in biotite compared to chlorite. Given that EPMA data indicate a $Fe^{3+}/\Sigma Fe_{biotite} = 0.26$, the estimated $Fe^{3+}/\Sigma Fe_{chlorite} = 0.08$ appears consistent with the redox contrast observed on the STXM-XANES transect.

Altogether, the data collected in the present study suggest that the biotite alteration observed in the investigated sample most likely involved the consumption of H_2 rather than production. Among other factors, this limited H_2 potential appears to stem primarily from the high initial biotite $Fe^{3+}/\Sigma Fe$ ratio, which significantly reduces the Fe^{2+} budget available for H_2 generation.

5.2. Radiolysis as a Direct Pathway for H_2 Generation

5.2.1. The Co-Occurrence of H_2 and ^4He

Radiolysis is widely recognized as a key process responsible for H_2 generation in intracontinental settings (Lin et al., 2005a; Sherwood Lollar et al., 2014; Warr et al., 2019), particularly where granites constitute the basement. In the Yorke Peninsula, elevated concentrations of helium were evidenced alongside H_2 during recent exploration drilling, suggesting a radiolytic origin for the H_2. In the studied sample, H_2 co-occurs with He presenting $^3He/^4He$ ratios ranging from 0.0003 to 0.0056 R/Ra (see gas results in Section 4.2). Such ratios are typical of those reported in rocks having granite-like compositions (e.g., Ballentine & Burnard, 2002), where the ^4He budget is dominated by in situ alpha decay of U, Th and Sm, whereas ^3He is primarily produced by nucleogenic reactions involving thermal neutron capture by ^6Li (Blard, 2021). In this regard, the similar ^4He concentrations observed in the two analyzed slabs (0.88 $\mu mol \cdot kg^{-1}_{rock}$ in the mafic slab and 0.70 $\mu mol \cdot kg^{-1}_{rock}$ in the felsic) highlight the homogeneity of ^4He content within the sample at first order. On the contrary, ^3He concentrations are markedly more heterogeneous between the two slabs (6.79×10^{-9} $\mu mol \cdot kg^{-1}_{rock}$ in the mafic slab and 2.99×10^{-10} $\mu mol \cdot kg^{-1}_{rock}$ in the felsic slab), which may reflect higher ^6Li contents in the mafic slab (e.g., hosted in biotite). This finding supports the interpretation that at least part of the H_2 in the sample may be derived from radiolysis within the Hiltaba Suite granite. From a geochemical perspective, the U, Th, and K contents in the sample (2.57 ppm, 20.81 ppm, and 2.91 wt%, respectively) are not exceptionally high compared to typical granitic rocks and the average continental crust (Hu & Gao, 2008). However, assessing the reality of radiolytic H_2 generation over geological timescales requires proper quantitative calculations accounting for the observed H_2 and He concentrations reported in these rocks of the Yorke Peninsula.

5.2.2. Quantitative Assessment of H_2 (and ^4He) Generation Rates From Radiolysis

Since the early 21st century, several studies have attempted to estimate radiolytic H_2 and ^4He co-generation rates over geological timescales based on the physicochemical properties of U-, Th-, and K-bearing rocks (Ballentine & Burnard, 2002; Lin et al., 2005a, 2005b; Sherwood Lollar et al., 2014; Warr et al., 2019). Even though the underlying equations rely on strong assumptions and idealized conditions (e.g., uniformly distributed porosity without a fracture network, complete pore-space saturation with water within the rock), they provide valuable first-order estimates of radiolytic H_2 and ^4He generation rates. Based on these foundational equations, a recent study introduced a statistical approach using Monte Carlo simulations to assess not only mean H_2 and ^4He generation rates but also the associated probability distributions (Warr et al., 2023). This methodology accounts for the inherent variability and complexity of natural samples by incorporating ranges for input parameters rather than single fixed values, thereby yielding the most probable generation rates under realistic geological conditions.

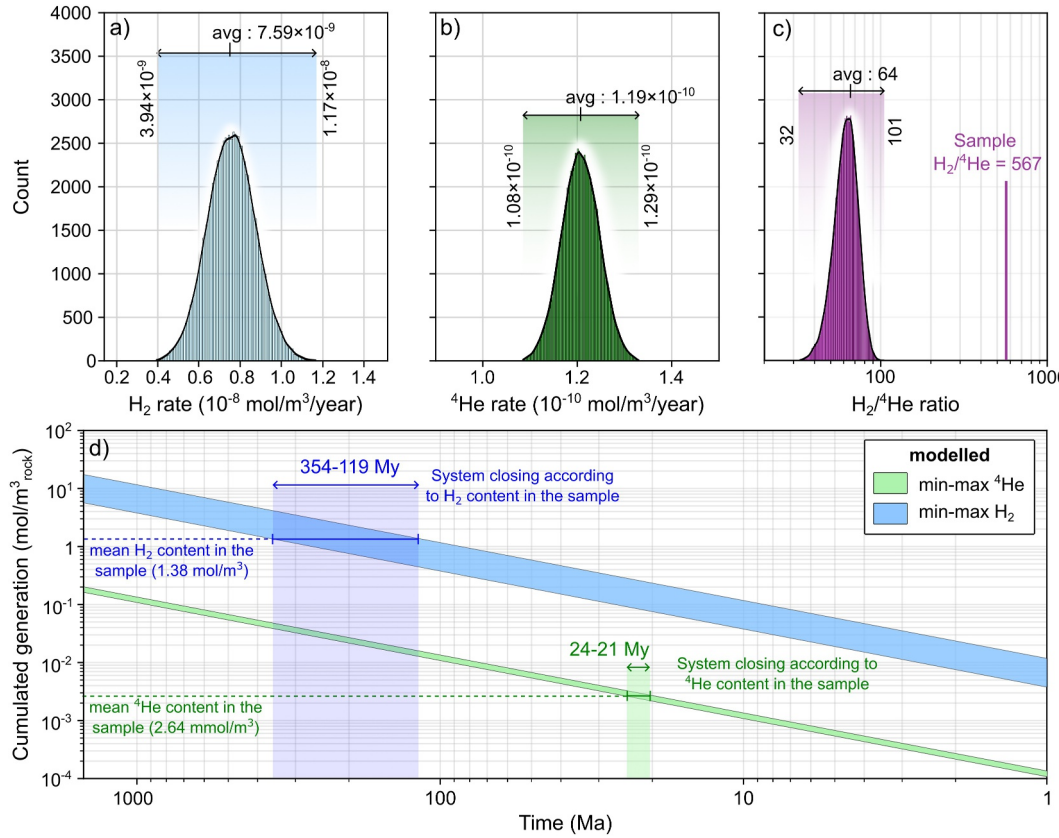

Figure 7. Simulation outputs of ^{4}He and H_2 generation by radiolysis of the studied sample, based on the methodology of Warr et al. (2023). (a–c) Histograms showing the probability density distributions of H_2 and ^{4}He generation rates, as well as the $H_2/^4$He ratio. (d) Logarithmic-scale plot illustrating the cumulated H_2 and ^{4}He generation yields over time, with shaded areas representing the modeled minimum and maximum bounds. Estimated system closure times can be inferred by comparing modeled yields to the measured H_2 and ^{4}He contents in the sample.

In the present study, we applied the methodology and equations outlined by Warr et al. (2023) to estimate the indigenous (i.e., in situ) H_2 and ^{4}He generation rates for our sample (see the original publication for a comprehensive description of the methodology). A custom Python script (provided in Figure S2 in Supporting Information S1) was developed for this purpose, and 10^5 simulations were performed using the following input parameters:

1. **The concentrations of U (2.57 ppm), Th (20.81 ppm), and K (2.91 wt%) in the studied sample** were determined by bulk rock analysis. For K, the proportion of the radioactive isotope (^{40}K) is incorporated in the radiolytic generation equations considering a ^{40}K/ΣK ratio of 0.012 (Draganić et al., 1991).
2. As **the density of the sample** is unknown, a range of plausible values **from 2.7 to 3.2 g/cm^3** was considered, following Warr et al. (2023). While the upper limit of 3.2 g/cm^3 may exceed that of a typical granite, it is justified by the high content of mafic minerals observed in the sample.
3. As **the density of the circulating fluid** is also unknown and may have varied over time due to fluctuations in salinity and/or temperature, a range **from 1.00 to 1.22 g/cm^3** was considered, in accordance with the parameters proposed by Warr et al. (2023).
4. As **the porosity of the sample** is unknown, a range **from 0.55% to 1.45%** was considered, consistent with values reported for similar upper crustal rocks (see Warr et al. (2023) and references therein).

Simulation results indicate possible generation rates ranging from 0.39 to 1.17×10^{-8} mol·kg^{-1} yr^{-1} for H_2 and from 1.08 to 1.29×10^{-10} mol·kg^{-1} yr^{-1} for ^{4}He. The average rates are 7.59×10^{-9} and 1.19×10^{-10} mol·kg^{-1} yr^{-1}, respectively (Figures 7a and 7b). Regarding the probability density distribution of the $H_2/^4$He ratio, the simulations yield a range between 32 and 101, with an average ratio of 64 (Figure 7c). Interestingly, the measured H_2 and ^{4}He concentrations in our sample are 0.46 mmol/kg and 0.883 μmol/kg, respectively (see Section 4.2). They correspond

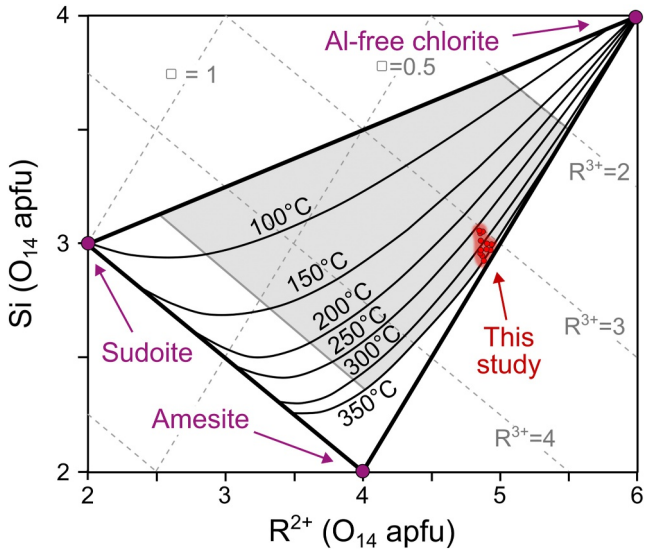

Figure 8. Graphical representation of the chlorite geothermometer developed by Bourdelle and Cathelineau (2015), based on the Si^{4+} and $R^{2+}(Mg^{2+} + Fe^{2+})$ contents in the chlorite formula unit. Chlorite compositions calculated from EPMA data in this study are shown in red, displaying relatively consistent values, although falling near the edge of the model's reliability range.

to an $H_2/^4He$ ratio of 567, which lies well above the range predicted by the simulations. This discrepancy suggests that additional geological processes beyond indigenous radiolysis may influence the observed H_2 and ^4He concentrations. These might involve, for instance, preferential He loss or H_2 gain, which would modify the expected $H_2/^4He$ ratio compared to a purely closed system. The following section discusses the factors controlling the $H_2/^4He$ ratio in the sample, addressing the questions of open- versus closed-system behavior, and indigenous gas production versus external gas supply.

5.3. Questioning the System's Dynamics: Open or Closed?

5.3.1. Timing of Last System Opening Estimated From the Temperature of the Last Brine Circulation

Constraining the timing of the last brine circulation in the sample is key to assessing how long it has remained isolated and whether its gas content is of indigenous origin. At least one brine circulation episode occurred within the sample, as indicated by the presence of planar arrays of liquid-rich fluid inclusions corresponding to healed microcracks (Figure 4). These microcracks, as well as the irregular shapes of the associated fluid inclusions, are commonly attributed to "late" fluid circulation events, in contrast to "early" events that typically produce negative-crystal-shaped fluid inclusions (Van Den Kerkhof & Hein, 2001). As discussed by these authors, however, the distinction between "early" and "late" fluid circulation episodes provides only a relative chronology of fluid inclusion trapping and does not strictly constrain the temperature of fluid circulation.

On the contrary, low-temperature brine circulation in the studied sample is highlighted by sericitized plagioclase and chloritized biotite, two alteration processes likely correlated in time in our sample, as previously discussed (see Section 5.1.3). Sericitization of plagioclase is a common low-temperature alteration process in granitic rocks, typically occurring during open-system epithermal alteration at $T < 300$°C (Morad et al., 2010; Rogers, 1916; Verati & Jourdan, 2014). Biotite chloritization is observed over a wider range of pressure-temperature conditions, spanning from early diagenesis to high-grade metamorphism. Chloritization temperatures as low as 50°C have been reported (Bourdelle, Benzerara, et al., 2013; Bourdelle, Parra, et al., 2013).

An initial estimate for the temperature of biotite chloritization in our sample was obtained using a graphical geothermometer developed by Bourdelle and Cathelineau (2015). It estimates low-temperature chlorite formation conditions based on Si^{4+} and R^{2+} contents (where $R^{2+} = Mg^{2+} + Fe^{2+}$). The resulting temperatures, although falling near the limits of the diagram's reliability, provide homogeneous values ranging between 250°C and 350°C (Figure 8). To refine this estimate, a quantitative geothermometer was applied based on chlorite formula units and its thermodynamic properties. Among the various thermodynamic-based chlorite geothermometers available in the literature (Bourdelle, Benzerara, et al., 2013; Bourdelle, Parra, et al., 2013; Inoue et al., 2009; Lanari et al., 2014; Vidal, 2005; Vidal et al., 2016), the model proposed by Inoue et al. (2018) was selected for this study because: (a) it was calibrated using natural chlorite samples within the 50–400°C temperature range, which presumably aligns with the conditions of interest here; and (b) it can be used assuming $\Sigma Fe = Fe^{2+}$. This latter assumption simplifies the thermodynamic calculations and is justified by the low Fe^{3+} content of the investigated chlorite ($Fe^{3+}/\Sigma Fe_{chlorite} = 0.08$; see Section 5.1.3). The calculations (available in Table S3; for a detailed description of the methodology, refer to Inoue et al. (2018)) yield a mean chlorite formation temperature of 351 ± 39°C (standard deviation calculated from the 11 chlorite formula units), which is slightly higher than the graphical estimate. The consistent temperature estimates from both geothermometers suggest a single fluid circulation event. Since the alteration is incomplete (i.e., primary biotite is not fully pseudomorphed by chlorite), this episode likely represents the most recent hydrothermal event recorded by the sample.

The estimated temperature of chlorite formation is not representative of the current thermal state of the studied sample, which was collected at a depth of only ~200 m. Given that South Australia is part of a stable cratonic region that has not experienced significant geodynamic activity since the Delamerian Orogeny at ~500 Ma

(Haines & Flöttmann, 1998), a typical cratonic geothermal gradient of ∼30°C/km can be assumed. This suggests that the brine responsible for biotite alteration must have circulated at depths of ∼10 km to reach temperatures around 300°C. Erosion rate estimates for the Yorke Peninsula remain poorly constrained and have likely varied greatly over the last ∼500 Ma depending on the dominant erosional regime (ranging from ∼510 m/Ma for glacial erosion to ∼0.32 m/Ma for subaerial erosion; Wilner et al., 2024). Regardless of the specific erosion rate, the 300°C fluid circulation episode recorded in the sample must be ancient, assuming that no external fluid warmer than the surrounding rocks have circulated. For example, using the mean continental erosion rate since the beginning of the Phanerozoic (estimated at 16 ± 11 m/Ma; Wilkinson & McElroy, 2007), a minimum of ∼370 Ma would be required to erode 10 km and overburden and exhume the Hiltaba Suite granite sampled in this study. Without drawing a definitive conclusion on the exact age of the last brine circulation, this first-order analysis provides evidence that the sample has remained in a closed state (i.e., without active fluid circulation and advection) for the last hundreds of millions of years. Consequently, at least part of the H_2 and He content in the sample can be considered to be of indigenous origin.

5.3.2. Significance of H_2 and ^{4}He Contents in the Sample

Using the minimum and maximum H_2 and He generation rates derived from the simulations, cumulative generation yields over time were estimated (Figure 7d). The measured H_2 and ^{4}He contents in the sample (0.46 mmol/kg and 0.883 μmol/kg respectively) were converted to mol/m^3 by considering a range of plausible rock densities from 2.7 to 3.2 g/cm^3. Assuming that all the measured H_2 and ^{4}He are of indigenous origin, a comparison of the simulated yields with the measured concentrations (1.24–1.52 mol/m^3 for H_2 and 2.38–2.91 mmol/m^3 for ^{4}He) allows for an estimation of the time elapsed since theoretical system closure. The H_2 content suggests a closure age between 354 Ma and 119 Ma, while the ^{4}He content suggests a significantly younger closure age between 24 Ma and 21 Ma (Figure 7d). This discrepancy underlines the previously noted divergence between the simulated and measured $H_2/^4$He ratios (Figure 7c). Several hypotheses can be discussed to explain this offset, some of which require a semi-open system:

1. **Indigenous radiolytic ^{4}He and H_2 generation may have been supplemented by indigenous H_2 enrichment from an unconstrained process.** H_2 production from Fe oxidation has been ruled out for this sample (see Section 5.1). However, other indigenous processes not investigated here may contribute to the overall H_2 budget. In particular, the production of H_2 during the decomposition of NH_3/NH_4^+ into N_2 has been proposed to explain the co-occurrence of N_2 in hydrothermal H_2-rich systems (Jacquemet & Prinzhofer, 2024; L. Li et al., 2009). Interestingly, gas chromatography after crushing revealed that our sample is N_2-rich, which is consistent with previous studies reporting that nitrogen is commonly found in H_2-rich Precambrian rocks in various redox forms, such as N_2, NO_3^-, NH_3/NH_4^+. The origin of nitrogen in these environments remains debated and may result from various processes, including meteoric fluid circulation or the destabilization of NH_4^+-rich minerals (Karolytė et al., 2022; L. Li et al., 2021; Silver et al., 2012). Although information is currently insufficient to determine the exact source of nitrogen in our sample, the absence of CO_2 and CH_4 suggests a non-meteoric origin. On the contrary, the high biotite content—a phyllosilicate known to incorporate significant amounts of NH_4^+ (Bos et al., 1988; Honma & Itihara, 1981)—supports an indigenous N_2 origin potentially associated with H_2 production. Regardless of the specific additional H_2-producing process involved, this hypothesis could explain the relative H_2 enrichment. If the system had remained fully closed since the last fluid circulation episode, such processes would have led to an increase in the $H_2/^4$He ratio relative to a purely radiolytic origin, aligning with our observations (Figure 7c). However, under this closed-system assumption, the age of system closure would be dictated by the ^{4}He content, estimated at only 21–24 Ma (Figure 7d). This does not correlate with the timing of the last fluid circulation episode, estimated at several hundreds of millions of years based on the biotite chloritization temperature (see Section 5.3.1). Therefore, additional mechanisms involving open-system behavior must be considered, where H_2 and ^{4}He can be lost or gained via migration.
2. **Indigenous radiolytic ^{4}He and H_2 generation may have been supplemented by external H_2-dominated enrichment from an unconstrained process.** The results of our investigation, focused on a single sample, provide no constraints on H_2 and He production pathways in the surrounding rocks. In this regard, external gas production followed by migration into our sample is plausible, occurring through either diffusion or advection. Assuming an external gas input dominated by H_2, this scenario would also provide a realistic explanation for the high $H_2/^4$He ratio measured compared to what would be expected from purely indigenous radiolysis

(Figure 7c). However, if the external gas input consisted only of H_2, this scenario would imply a maximum system closure age of 24–21 Ma, as indicated by the radiogenic ^{4}He content of the sample (Figure 7d). Any enrichment of ^{4}He in the external gas would add to the indigenous radiolytic ^{4}He, further reducing the estimated age of system closure. As with the scenario (1), such timing for system closure is ruled out by the age estimated from biotite chloritization, which is thought to have occurred several hundreds of millions of years ago.

3. **The measured H_2 and ^{4}He contents may reflect radiolytic generation within the studied sample, with differential diffusion leading to preferential He loss over time.** Both previous scenarios proposed additional H_2 enrichment—from either indigenous or external sources—to explain the very high $H_2/^4$He ratio measured in the sample. However, they fail to reconcile the timing of system closure estimated from biotite chloritization (>370 Ma) with the actual amount of ^{4}He found in the sample. Therefore, a third scenario is proposed, in which the indigenous radiolytic ^{4}He is continuously lost at a faster rate than radiolytic H_2 since the last fluid circulation episode several hundreds of millions of years ago. In fact, this apparent system closure would not preclude the thermal diffusive loss of gases over time, that may have occurred under 300°C. This hypothesis is supported by the fact that, due to its smaller atomic size ^{4}He have a larger diffusivity than H_2 in silicates under these low temperature conditions (Cherniak & Watson, 2011; Farley, 2000; Ingrin, 2006). This scenario (3) provides a single mechanism to explain both the relative H_2 enrichment compared to ^{4}He, and the low amounts of ^{4}He relative to the proposed timing of the last fluid circulation.

At this stage, it is clear that no definitive conclusion can be drawn to explain the sample's gas signature. The three mechanisms proposed above represent simplified conditions that might occur concomitantly in the complex reality of the natural environment.

5.3.3. Implications for Gas Migration in the Yorke Peninsula: Diffusion Instead of Advection?

From a general perspective, it is important to note that the Yorke Peninsula is crosscut by numerous crustal-scale faults (Figure 1). These faults may act locally as preferential conduits for advective migration and gas accumulation in the overlying sedimentary cover. In the present investigation, however, no direct evidence of such active and recent fluid circulation was observed. Specifically, the elevated temperatures estimated for the last fluid circulation episode suggest a system closure age >370 Ma (see Section 5.3.1). This result casts doubt on a scenario where advection is the primary mechanism responsible for H_2 and ^{4}He migration from the studied basement sample to the overlying sedimentary rocks. In addition, the >370 Ma estimate is not significantly different from the closure age estimated from H_2 concentrations (354-119 Ma), but exceeds the closure age of ^{4}He (24-21 Ma), as discussed in Section 5.2.2. Regardless of whether the H_2 and He contents in the sample are entirely of indigenous origin or partly from an external source, this age comparison supports the hypothesis of a long-term diffusive gas migration inducing a preferential He loss (over H_2) over the last several hundreds of millions of years. This interpretation is in line with the higher diffusivity of ^{4}He relative to H_2 in silicates (Cherniak & Watson, 2011; Farley, 2000; Ingrin, 2006). In addition, this scenario is also consistent with the significant He enrichment reported in some horizons of the sedimentary cover (^{4}He up to 6.8% once corrected for air contamination, see Whitcombe et al. (2024)). This outcome contrasts sharply with the ratios obtained in this study: a measured $H_2/^4$He ratio of 567 in the sample and simulated $H_2/^4$He ratios from 32 to 101. Altogether, the evidence collected here points toward diffusive-dominated migration of ^{4}He from the bedrock to the sedimentary cover in the area where the sample was collected. This interpretation does not preclude a significant contribution of advective-dominated migration elsewhere in the Yorke Peninsula, particularly where crustal-scale faults occur.

5.4. Summary of the Sample History

The comprehensive petrographic characterization of the sample provides the basis for proposing the key stages of its history within the framework of H_2 and ^{4}He exploration. These stages can be summarized as follows:

1. **Emplacement of the Hiltaba Suite granite intrusions (~1.5 Ga).** Primary paragenesis is dominated by biotite, amphibole, pyroxene, quartz, feldspar, titanite, and magnetite. Crystallization conditions during cooling (e.g., oxygen fugacity) imply that biotite, the main Fe^{2+}-bearing primary mineral, incorporates a significant proportion of Fe^{3+} (see Section 5.1.2). Based on our interpretations, the sample does not record any geodynamic of geological activity for the following ~1.0 Ga.

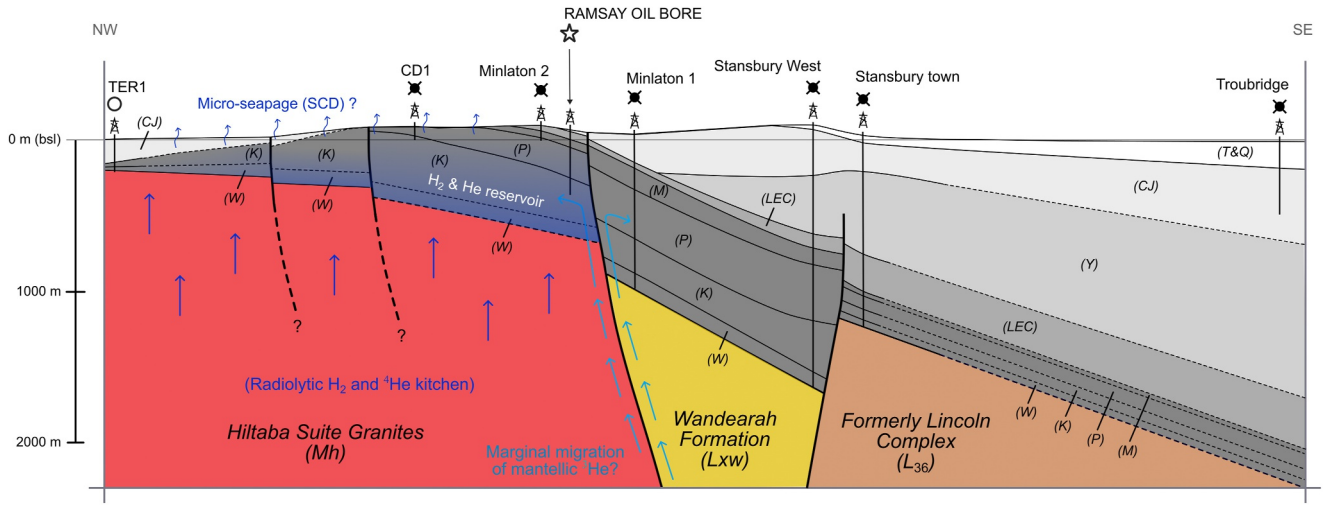

Figure 9. NW-SE cross-section of the geology in the Yorke Peninsula. The exact location of the transect is reported in Figure 1. Red, yellow and brown colors represent basement units, as presented in Figure 1. The sedimentary cover, from Cambrian to Quaternary in age, is represented from dark gray to white color. Abbreviations: (W), early Cambrian Winulta Fm; (K), early Cambrian Kulpara Fm; (P), early Cambrian Parara Fm; (M), early Cambrian Minlaton Fm; (LEC), undifferentiated late early Cambrian units; (Y), middle Cambrian Yuruga Fm; (CJ), Permian Cape Jervis Fm; (T&Q), undifferentiated Tertiary and Quaternary units. Following the drillhole data available and this study, the H_2- and He-rich accumulations are expected to occur in the early Cambrian horizons above the Hiltaba Suite granites.

2. **Water-rock interaction and last system opening (>370 Ma).** A fluid circulation event, the last recorded in the sample, accompanied by chloritization of biotite and sericitization of feldspars, occurred at approximately 300–400°C. The uniform temperatures provided by the chlorite geothermometer suggest a single episode of fluid circulation (see Section 5.3.1). Assuming standard crustal erosion rates and geothermal gradients, the temperature event infers an age as recent as 370 Ma. During this fluid circulation episode, the system was opened, allowing the advective release of H_2 and ^{4}He previously generated by radiolysis and other processes, and accumulated within the sample. The chloritization of biotite involved a slight H_2 consumption instead of generation, highlighted by the reduction of Fe^{3+} during the reaction (see Section 5.1.3).
3. **H_2 and He generation and loss through diffusion (<370 Ma).** Following the last circulation event, H_2 and ^{4}He generation continued within the system, essentially via radiolysis. Concomitantly, H_2 and ^{4}He have been continuously lost out from the system through passive diffusion. This ongoing diffusive loss is reflected in the measured H_2 and He contents, which suggest younger apparent ages for the last system opening than those inferred from the temperature of the last fluid circulation event (see Section 5.3.1). As ^{4}He loss operates faster than H_2 loss, the apparent age of the last system opening appears younger for ^{4}He than H_2. Both gas losses ultimately feed the overlying accumulations in the sedimentary cover.

5.5. Perspectives for the Strategy of H_2 and He Exploration in South Australia

Following the drilling of the Ramsay Oil Bore in 1933, the Minlaton-1 well was drilled nearby. Surprisingly, no H_2 was detected at Minlaton-1, although it intersected the same sedimentary units as the Ramsay Oil Bore (Figure 9). This apparent discrepancy in H_2 occurrence between the Ramsay Oil Bore and Minlaton-1 may be attributed to differences in the underlying basement lithologies. Specifically, it suggests a greater H_2 generating potential for the Hiltaba granite compared to other basement units, such as the metasedimentary Wandearah Formation, as previously proposed by Boreham, Edwards et al. (2021) and Boreham, Sohn et al. (2021).

Concerning the H_2 source rock, the petrographic investigation presented here provides evidence that the Hiltaba Suite Granite likely contributes to the overall H_2 budget in the Yorke Peninsula, through radiolytic production from U-Th-K decay. Interestingly, ^{3}He/^{4}He ratios have been reported from recent drillings conducted close to the historical Ramsay Oil Bore (see https://www.goldhydrogen.com.au/asx-releases/helium-3-confirmed-at-ramsay-project/). At Ramsay 1, three ^{3}He/^{4}He ratios were measured in the basement ($n = 1$) and the Kulpara Formation ($n = 2$), all from He-rich horizons. Remarkably consistent values of 0.0069 R/Ra, 0.0067 R/Ra, and 0.0067 R/Ra were obtained, similar to one of the ratios measured in our sample (0.0056 ± 0.0005 R/Ra), supporting a radiolytic origin. At Ramsay 2, six ^{3}He/^{4}He ratios were measured in the basement ($n = 1$), the Kulpara Formation ($n = 2$),

and the Parara Formation ($n = 3$). The only He-rich horizon, located in the Kulpara Formation, showed a $^{3}He/^{4}He$ ratio of 0.0066 R/Ra. This result, consistent with the Ramsay 1 measurements, also supports a radiolytic origin. In contrast, the five other horizons, which are comparatively He-poor and H_2-rich, display highly variable $^{3}He/^{4}He$ ratios ranging from 0.0489 to 1.2306 R/Ra. This relative ^{3}He enrichment, with ratios approaching ~1 R/Ra only in He-poor samples, points to possible atmospheric contamination, for instance during sampling. Alternatively, a mantle-derived ^{3}He contribution to the overall gas fluxes cannot be excluded at this stage. In this scenario, the presence of a regional fault near the Ramsay Oil Bore may act as a migration pathway for mantle-sourced ^{3}He (Figure 9). Complementary ^{20}Ne measurements would enable quantitative correction for atmospheric helium, given that ^{20}Ne is mostly atmospheric in origin and serves as a sensitive tracer of air contamination, thereby providing a robust test of whether the observed $^{3}He/^{4}He$ ratios reflect air contamination or a mantle-derived contribution.

Concerning the H_2 reservoir rocks, among the numerous exploration wells drilled across the Peninsula, only the Ramsay Oil Bore revealed H_2- and He-rich horizons. These accumulations are located directly above the Hiltaba Suite granite, specifically in areas where the early Cambrian sediments of the Kulpara and Parara Formations are the thickest (Figure 9). This spatial correlation suggests that westward exploration for subsurface accumulation may appear irrelevant, if the progressive thinning of the sedimentary cover compromises the presence and effectiveness of H_2 and He reservoir-and-seal formations. For instance, the Parara Formation, which contains alternating layers of mudstones and limestone recognized elsewhere to favor He sequestration in aquifers (e.g., Marty et al., 2003), is mostly absent in the western part of the Peninsula. Reciprocally, the search for surficial H_2 micro-seepages (e.g., sub-circular depressions) in the western part of the Peninsula, where the sedimentary cover is thinner, may appear promising as already proposed in the literature (Moretti et al., 2021). Noteworthy, the accumulations reported from shallower subsurface horizons intersected by the Ramsay wells contain H_2, He, and N_2 but also additional components such as CH_4 and, locally, minor CO_2 (Boreham, Edwards, et al., 2021). In contrast, the gas composition identified in the analyzed basement sample is limited to H_2, He, and N_2. This compositional difference highlights that the shallow blended gas composition cannot be explained solely by generation within the underlying crystalline basement. Secondary processes that modify the primary gas signature during upward migration and trapping must therefore be invoked to account for the presence of CO_2 and CH_4. For instance, the occurrence of minor CO_2 may be related to the carbonate-dominated nature of the reservoir rocks (e.g., the dolomite of the Kulpara Formation), whereas the presence of CH_4 may result from low-temperature biogenic consumption of H_2 by the deep biosphere (Nothaft et al., 2026) and/or mixing with CH_4 generated by thermogenic processes (Etiope & Sherwood Lollar, 2013). At this stage, these hypotheses remain provisional and will require validation through additional studies.

The findings presented here provide global perspectives for natural H_2 and He exploration in South Australia (SA), where numerous exploration blocks are currently under investigation. The presence of H_2 within fluid inclusions in the TER1 drill core sample echoes the recent reporting of H_2-rich fluid inclusions in Hiltaba Suite granites from other locations across SA (Bourdet et al., 2023). Occurrences of Hiltaba Suite granites are widespread in SA, representing more than 28,500 km^2 according to basement geology maps (see Maitland SI5312 geological map of the Department for Energy and Mining SA). Extrapolating petrographic observations from a single drill core to the entire extent of the Hiltaba Suite appears highly speculative, particularly given the expected variability in composition and alteration grades depending on the nature and history of the intrusions. However, our results highlight that Hiltaba Suite Granite is a promising lithology to prospect H_2 and He accumulations. As such, this rock unit warrants focused attention in ongoing and future gas exploration efforts across the region.

5.6. Limitations of the Study and Perspectives for Future Works

The interpretations detailed here provide an initial step toward addressing the timing and pathways of H_2 (and He) generation and subsequent migration—factors that are essential for constraining the origin of entrapped gases and evaluating the resource potential. However, the current discussion is derived from several assumptions that must be viewed with caution, given the inherent limitations of this study. In particular, the chloritization temperature was used to provide first-order estimates of the age of the last fluid circulation episode. This study would have benefited from a more robust temperature estimate by cross-comparing results from the chlorite geothermometer with another independent proxy (e.g., $\delta^{18}O$ of H_2O–quartz in fluid inclusions; Bourdet et al., 2023). Furthermore, absolute age constraints using radiochronological dating would have been more reliable. The formation of chlorite can hardly be dated directly. However, dating titanite precipitation during biotite chloritization offers a

promising perspective, as titanite typically incorporates U, enabling the use of U/Pb techniques (e.g., Simonetti et al., 2006). In addition, only two H_2-generating mechanisms were deeply investigated in this study: radiolysis and Fe-oxidation. This does not preclude a possible contribution from one or several additional sources (e.g., NH_4^+ decomposition; Jacquemet & Prinzhofer, 2024), which will be worth investigating in future studies. Finally, the present interpretations are derived from petrographic data acquired from a single drill core sample and therefore do not capture the heterogeneities that may occur in natural environments (e.g., variable rock compositions or alteration grades). Such heterogeneities are expected to significantly influence the models of H_2 and ^{4}He generation via radiolysis (and other generation processes), as well as surmised migration pathways. For instance, the absence of any fluid circulation event for several hundred million years, as estimated from the studied sample, implies that gas migration into and out of the studied sample has only operated through diffusion. This does not preclude the occurrence of more recent circulation events elsewhere in the Hiltaba Suite Granite, particularly in structurally complex areas where fault networks are more extensively developed.

Altogether, there is no doubt that the current data set is insufficient to draw definitive large-scale conclusions; further work is therefore required to advance our understanding of gas formation and accumulation processes in this region. Specifically, additional petrographic investigations are needed to better characterize the lithological and alteration heterogeneities within the intrusive Hiltaba Suite.

6. Conclusions

Natural H_2 is increasingly being investigated as a potential contributor to achieve net-zero emission targets. Exploration programs are being developed, particularly in Australia, leading to recent and future drilling campaigns. The Yorke Peninsula, South Australia (SA), represents a unique case study to advance the understanding of H_2 systems—in terms of generation, migration and accumulation processes—as it is one of the few locations worldwide known to host natural H_2 accumulations both from historic and confirmed by recent drilling.

Through detailed petrographic and geochemical characterization of a drill core sample from the Hiltaba Suite Granite (TER1), which forms part of the crystalline basement of the Yorke Peninsula, this study provides new insights into the origin of H_2 and He in the region. Our results suggest that radiolysis is the predominant mechanism for H_2 and ^{4}He generation in this lithology, as evidenced by the presence of H_2-bearing fluid inclusions, and elevated concentrations of the two gases in the sample. The sample appears Fe^{2+}-rich and the alteration of biotite, the only primary Fe-bearing mineral altered, resulted in Fe mobilization and its incorporation into secondary Fe-oxide and chlorite. However, this transformation likely occurred without significant Fe oxidation, implying that Fe-driven H_2 generation did not significantly contribute to the H_2 budget in the sample.

The coupling of (a) ^{4}He and H_2 content measurements, (b) numerical modeling of radiolytic generation rates, and (c) chlorite-based geothermometry of the last circulation brine points to a system closure several hundred Ma ago (>370 Ma). This phase was presumably followed by a protracted diffusion-dominated migration of gas species. The discrepancy between estimated closure ages derived from H_2 and ^{4}He contents, as well as the $H_2/^4$He ratio, reinforces the hypothesis of differential diffusion rates between H_2 and ^{4}He, while also aligning with He enrichments observed in subsurface accumulations.

These findings identify the Hiltaba Suite as a compelling exploration target for H_2 and He exploration programs across the Yorke Peninsula and other regions of SA. However, the significant variability in lithology and alteration grades likely to occur across the >28,000 km^2 extent of the Hiltaba Suite precludes direct or simplistic extrapolation based on a single sample.

Conflict of Interest

The authors declare no conflicts of interest relevant to this study.

Availability Statement

Bulk geochemical analyses are provided in Table S1. Helium isotope measurements performed on the two sample slabs are available in Table S2. Raw EPMA data acquired on chlorite and used for calculations for mineral formula units and associated thermodynamic geothermometer are provided in Table S3. Details concerning

Cramer's system methodology used for reaction balancing are provided in Figure S1 in Supporting Information S1. Methodology for determination of $Fe^{3+}/\Sigma Fe$ in chlorite is developed in Text S1 in Supporting Information S1. The python script and the input/output data of the simulations performed to assess radiolytic H_2 and ^4He generation rates are provided in Figure S2 and Text S2 in Supporting Information S1. All the aforementioned data, available in Supporting Information S1, are also archived in a permanent and freely accessible repository at Geymond (2026).

Acknowledgments

All authors want to express their gratitude to Sophie Nowak (UPC), Nicolas Rividi (ISTeP), Arnaud Duverger (IMPMC), Valentine Megevand (IMPMC), Jean-Christophe Viennet (IMPMC) and Corentin Le Guillou (UMET) who particularly helped to perform analyses and process raw data from XRD, SEM, EPMA, TEM and STXM. The authors also thank the entire South Australia Core Library team, especially David Groom for the sampling process facilitations. Grateful acknowledgment is made to the editors, Marie Edmonds and Emma Nicholson, as well as Christopher Boreham and the second anonymous reviewer, whose constructive and insightful comments substantially improved the original manuscript. This work was funded by Gold Hydrogen Limited.

References

Ballentine, C. J., & Burnard, P. G. (2002). Production, release and transport of noble gases in the continental crust. *Reviews in Mineralogy and Geochemistry*, *47*(1), 481–538. https://doi.org/10.2138/rmg.2002.47.12

Belkhou, R., Stanescu, S., Swaraj, S., Besson, A., Ledoux, M., Hajlaoui, M., & Dalle, D. (2015). HERMES: A soft X-ray beamline dedicated to X-ray microscopy. *Journal of Synchrotron Radiation*, *22*(4), 968–979. https://doi.org/10.1107/S1600577515007778

Blard, P.-H. (2021). Cosmogenic ^{3}He in terrestrial rocks: A review. *Chemical Geology*, *586*, 120543. https://doi.org/10.1016/j.chemgeo.2021.120543

Boreham, C. J., Edwards, D. S., Czado, K., Rollet, N., Wang, L., van der Wielen, S., et al. (2021). Hydrogen in Australian natural gas: Occurrences, sources and resources. *The APPEA Journal*, *61*(1), 163–191. https://doi.org/10.1071/AJ20044

Boreham, C. J., Sohn, J. H., Cox, N., Williams, J., Hong, Z., & Kendrick, M. A. (2021). Hydrogen and hydrocarbons associated with the Neoarchean Frog's Leg Gold Camp, Yilgarn Craton, Western Australia. *Chemical Geology*, *575*, 120098. https://doi.org/10.1016/j.chemgeo.2021.120098

Bos, A., Duit, W., Van Der Eerden, A. M. J., & Jansen, J. B. H. (1988). Nitrogen storage in biotite: An experimental study of the ammonium and potassium partitioning between 1M-phlogopite and vapour at 2 kb. *Geochimica et Cosmochimica Acta*, *52*(5), 1275–1283. https://doi.org/10.1016/0016-7037(88)90281-5

Boucher, C., Lan, T., Mabry, J., Bekaert, D. V., Burnard, P. G., & Marty, B. (2018). Spatial analysis of the atmospheric helium isotopic composition: Geochemical and environmental implications. *Geochimica et Cosmochimica Acta*, *237*, 120–130. https://doi.org/10.1016/j.gca.2018.06.010

Bourdelle, F., Benzerara, K., Beyssac, O., Cosmidis, J., Neuville, D. R., Brown, G. E., & Paineau, E. (2013). Quantification of the ferric/ferrous iron ratio in silicates by scanning transmission X-ray microscopy at the Fe L2,3 edges. *Contributions to Mineralogy and Petrology*, *166*(2), 423–434. https://doi.org/10.1007/s00410-013-0883-4

Bourdelle, F., & Cathelineau, M. (2015). Low-temperature chlorite geothermometry: A graphical representation based on a T–R^{2+}–Si diagram. *European Journal of Mineralogy*, *27*(5), 617–626. https://doi.org/10.1127/ejm/2015/0027-2467

Bourdelle, F., Parra, T., Chopin, C., & Beyssac, O. (2013). A new chlorite geothermometer for diagenetic to low-grade metamorphic conditions. *Contributions to Mineralogy and Petrology*, *165*(4), 723–735. https://doi.org/10.1007/s00410-012-0832-7

Bourdet, J., Piane, C. D., Wilske, C., Mallants, D., Suckow, A., Questiaux, D., et al. (2023). Natural hydrogen in low temperature geofluids in a Precambrian granite, South Australia. Implications for hydrogen generation and movement in the upper crust. *Chemical Geology*, *638*, 121698. https://doi.org/10.1016/j.chemgeo.2023.121698

Castle-Jones, J., Betts, M. J., Holmes, J. D., Klaebe, R. M., Hall, P. A., Crowley, J. L., et al. (2025). Integrated biostratigraphy, chemostratigraphy and geochronology of the lower Cambrian succession in the western Stansbury Basin, South Australia. *Australian Journal of Earth Sciences*, *72*(2), 182–212. https://doi.org/10.1080/08120099.2025.2473098

Chen, Y., & Chou, I.-M. (2022). Determination of H_2 densities over a wide range of temperatures and pressures based on the spectroscopic characterization of Raman vibrational bands. *Applied Spectroscopy*, *76*(7), 841–850. https://doi.org/10.1177/00037028221080489

Cherniak, D. J., & Watson, E. B. (2011). Helium diffusion in rutile and titanite, and consideration of the origin and implications of diffusional anisotropy. *Chemical Geology*, *288*(3–4), 149–161. https://doi.org/10.1016/j.chemgeo.2011.07.015

Chou, I.-M., Burruss, R. C., & Lu, W. (2005). A new optical capillary cell for spectroscopic studies of geologic fluids at pressures up to 100 MPa. In J. Chen, Y. Wang, T. S. Duffy, G. Shen, & L. F. Dobrzhinetskaya (Eds.), *Advances in high-pressure technology for geophysical applications* (pp. 475–485). Elsevier. https://doi.org/10.1016/B9780444451979-5.50026-0

Combaudon, V., Sissmann, O., Bernard, S., Viennet, J.-C., Megevand, V., Le Guillou, C., et al. (2024). Are the Fe-rich-clay veins in the igneous rock of the Kansas (USA) Precambrian crust of magmatic origin? *Lithos*, *474–475*, 107583. https://doi.org/10.1016/j.lithos.2024.107583

Cotten, J., Le Dez, A., Bau, M., Caroff, M., Maury, R. C., Dulski, P., et al. (1995). Origin of anomalous rare-earth element and yttrium enrichments in subaerially exposed basalts: Evidence from French Polynesia. *Chemical Geology*, *119*(1–4), 115–138. https://doi.org/10.1016/0009-2541(94)00102-E

Doll, P., Eaves, S. R., Kennedy, B. M., Blard, P.-H., Nichols, A. R. L., Leonard, G. S., et al. (2024). Cosmogenic ^{3}He chronology of postglacial lava flows at Mt Ruapehu, Aotearoa/New Zealand. *Geochronology*, *6*(3), 365–395. https://doi.org/10.5194/gchron-6-365-2024

Draganić, I. G., Bjergbakke, E., Draganić, Z. D., & Sehested, K. (1991). Decomposition of ocean waters by potassium-40 radiation 3800 Ma ago as a source of oxygen and oxidizing species. *Precambrian Research*, *52*(3–4), 337–345. https://doi.org/10.1016/0301-9268(91)90087-Q

Eggleton, R., & Banfield, J. (1985). The alteration of granitic biotite to chlorite. *American Mineralogist*, *70*, 902–910.

Etiope, G., & Sherwood Lollar, B. (2013). Abiotic methane on Earth. *Reviews of Geophysics*, *51*(2), 276–299. https://doi.org/10.1002/rog.20011

Farley, K. A. (2000). Helium diffusion from apatite: General behavior as illustrated by Durango fluorapatite. *Journal of Geophysical Research*, *105*(B2), 2903–2914. https://doi.org/10.1029/1999JB900348

Flöttman, T., Haines, P. W., Cockshell, C. D., & Preiss, W. V. (1997). An early Palaeozoic foreland basin succession beneath Gulf St Vincent, South Australia? Implications for petroleum plays. *Petroleum Exploration Society of Australia Journal*, *25*.

Frezzotti, M. L., Tecce, F., & Casagli, A. (2012). Raman spectroscopy for fluid inclusion analysis. *Journal of Geochemical Exploration*, *112*, 1–20. https://doi.org/10.1016/j.gexplo.2011.09.009

Geymond, U. (2026). Radiolysis and Fe-biotite alteration: Questioning the origin of H_2-bearing fluid inclusions in the Yorke Peninsula granites, South Australia [Dataset] [Jeu de données]. *Zenodo*. https://doi.org/10.5281/ZENODO.18701216

Geymond, U., Loiseau, K., Roche, V., Pasquet, G., Revillon, S., Sougrati, M., & Moretti, I. (2025). Mössbauer spectroscopy: A key tool to quantify Fe-speciation and distribution in H_2-generating rocks. *Applied Geochemistry*, *187*, 106399. https://doi.org/10.1016/j.apgeochem.2025.106399

Godard, G. (2010). Two orogenic cycles recorded in eclogite-facies gneiss from the southern Armorican Massif (France). *European Journal of Mineralogy*, *21*(6), 1173–1190. https://doi.org/10.1127/0935-1221/2009/0021-1984

Gravestock, D. I., & Shergold, J. H. (2000). 6. Australian early and Middle Cambrian sequence biostratigraphy with implications for species diversity and correlation. In A. Zhuravlev & R. Riding (Éds.), *The ecology of the Cambrian radiation* (pp. 107–136). Columbia University Press. https://doi.org/10.7312/zhur10612-006

Gündüz, M., & Asan, K. (2023). MagMin_PT: An Excel-based mineral classification and geothermobarometry program for magmatic rocks. *Mineralogical Magazine*, *87*(1), 1-9–9. https://doi.org/10.1180/mgm.2022.113

Haines, P. W., & Flöttmann, T. (1998). Delamerian Orogeny and potential foreland sedimentation: A review of age and stratigraphic constraints. *Australian Journal of Earth Sciences*, *45*(4), 559–570. https://doi.org/10.1080/08120099808728412

Honma, H., & Itihara, Y. (1981). Distribution of ammonium in minerals of metamorphic and granitic rocks. *Geochimica et Cosmochimica Acta*, *45*(6), 983–988. https://doi.org/10.1016/0016-7037(81)90122-8

Hu, Z., & Gao, S. (2008). Upper crustal abundances of trace elements: A revision and update. *Chemical Geology*, *253*(3–4), 205–221. https://doi.org/10.1016/j.chemgeo.2008.05.010

Ingrin, J. (2006). Diffusion of hydrogen in minerals. *Reviews in Mineralogy and Geochemistry*, *62*(1), 291–320. https://doi.org/10.2138/rmg.2006.62.13

Inoue, A., Inoué, S., & Utada, M. (2018). Application of chlorite thermometry to estimation of formation temperature and redox conditions. *Clay Minerals*, *53*(2), 143–158. https://doi.org/10.1180/clm.2018.10

Inoue, A., Meunier, A., Patrier-Mas, P., Rigault, C., Beaufort, D., & Vieillard, P. (2009). Application of chemical geothermometry to low-temperature trioctahedral chlorites. *Clays and Clay Minerals*, *57*(3), 371–382. https://doi.org/10.1346/CCMN.2009.0570309

Jacquemet, N., & Prinzhofer, A. (2024). The association of natural hydrogen and nitrogen: The ammonium clue? *International Journal of Hydrogen Energy*, *50*, 161–174. https://doi.org/10.1016/j.ijhydene.2023.07.265

Karolytė, R., Warr, O., van Heerden, E., Flude, S., de Lange, F., Webb, S., et al. (2022). The role of porosity in H_2/He production ratios in fracture fluids from the Witwatersrand Basin, South Africa. *Chemical Geology*, *595*, 120788. https://doi.org/10.1016/j.chemgeo.2022.120788

Klein, F., Bach, W., & McCollom, T. M. (2013). Compositional controls on hydrogen generation during serpentinization of ultramafic rocks. *Lithos*, *178*, 55–69. https://doi.org/10.1016/j.lithos.2013.03.008

Lanari, P., Wagner, T., & Vidal, O. (2014). A thermodynamic model for di-trioctahedral chlorite from experimental and natural data in the system MgO–FeO–Al_2O_3–SiO_2–H_2O: Applications to P–T sections and geothermometry. *Contributions to Mineralogy and Petrology*, *167*(2), 968. https://doi.org/10.1007/s00410-014-0968-8

Le Guillou, C., Changela, H. G., & Brearley, A. J. (2015). Widespread oxidized and hydrated amorphous silicates in CR chondrites matrices: Implications for alteration conditions and H_2 degassing of asteroids. *Earth and Planetary Science Letters*, *420*, 162–173. https://doi.org/10.1016/j.epsl.2015.02.031

Leong, J. A., Nielsen, M., McQueen, N., Karolytė, R., Hillegonds, D. J., Ballentine, C., et al. (2023). H2 and CH4 outgassing rates in the Samail ophiolite, Oman: Implications for low-temperature, continental serpentinization rates. *Geochimica et Cosmochimica Acta*, *347*, 1–15. https://doi.org/10.1016/j.gca.2023.02.008

Li, L., Cartigny, P., & Ader, M. (2009). Kinetic nitrogen isotope fractionation associated with thermal decomposition of NH_3: Experimental results and potential applications to trace the origin of N_2 in natural gas and hydrothermal systems. *Geochimica et Cosmochimica Acta*, *73*(20), 6282–6297. https://doi.org/10.1016/j.gca.2009.07.016

Li, L., Li, K., Giunta, T., Warr, O., Labidi, J., & Sherwood Lollar, B. (2021). N_2 in deep subsurface fracture fluids of the Canadian Shield: Source and possible recycling processes. *Chemical Geology*, *585*, 120571. https://doi.org/10.1016/j.chemgeo.2021.120571

Li, L., Zhang, X., Luan, Z., Li, Y., Li, Y., Wang, B., et al. (2018). Raman vibrational spectral characteristics and quantitative analysis of H_2 up to 400°C and 40 MPa. *Journal of Raman Spectroscopy*, *49*(11), 1722–1731. https://doi.org/10.1002/jrs.5420

Li, X., Zhang, C., Behrens, H., & Holtz, F. (2020). Calculating biotite formula from electron microprobe analysis data using a machine learning method based on principal components regression. *Lithos*, *356–357*, 105371. https://doi.org/10.1016/j.lithos.2020.105371

Lin, L.-H., Slater, G. F., Sherwood Lollar, B., Lacrampe-Couloume, G., & Onstott, T. C. (2005a). Radiolytic H_2 in continental crust: Nuclear power for deep subsurface microbial communities. *Geochimica et Cosmochimica Acta*, *69*(4), 893–903. https://doi.org/10.1029/2004GC000907

Lin, L.-H., Slater, G. F., Sherwood Lollar, B., Lacrampe-Couloume, G., & Onstott, T. C. (2005b). The yield and isotopic composition of radiolytic H_2, a potential energy source for the deep subsurface biosphere. *Geochimica et Cosmochimica Acta*, *69*(4), 893–903. https://doi.org/10.1016/j.gca.2004.07.032

Marcaillou, C., Muñoz, M., Vidal, O., Parra, T., & Harfouche, M. (2011). Mineralogical evidence for H_2 degassing during serpentinization at 300°C/300bar. *Earth and Planetary Science Letters*, *303*(3–4), 281–290. https://doi.org/10.1016/j.epsl.2011.01.006

Marty, B., Dewonck, S., & France-Lanord, C. (2003). Geochemical evidence for efficient aquifer isolation over geological timeframes. *Nature*, *425*(6953), 55–58. https://doi.org/10.1038/nature01966

McCollom, T. M., Klein, F., Moskowitz, B., Berquó, T. S., Bach, W., & Templeton, A. S. (2020). Hydrogen generation and iron partitioning during experimental serpentinization of an olivine–pyroxene mixture. *Geochimica et Cosmochimica Acta*, *282*, 55–75. https://doi.org/10.1016/j.gca.2020.05.016

Megevand, V., Viennet, J.-C., Le Guillou, C., Guyot, F., & Bernard, S. (2025). Tardi-magmatic iddingsite in the Martian Nakhlite NWA 817. *Geochimica et Cosmochimica Acta*, *393*, 318–333. https://doi.org/10.1016/j.gca.2025.01.028

Morad, S., El-Ghali, M. A. K., Caja, M. A., Sirat, M., Al-Ramadan, K., & Mansurbeg, H. (2010). Hydrothermal alteration of plagioclase in granitic rocks from Proterozoic basement of SE Sweden. *Geological Journal*, *45*(1), 105–116. https://doi.org/10.1002/gj.1178

Moretti, I., Brouilly, E., Loiseau, K., Prinzhofer, A., & Deville, E. (2021). Hydrogen emanations in intracratonic areas: New guide lines for early exploration basin screening. *Geosciences*, *11*(3), 145. https://doi.org/10.3390/geosciences11030145

Murray, J., Clément, A., Fritz, B., Schmittbuhl, J., Bordmann, V., & Fleury, J. M. (2020). Abiotic hydrogen generation from biotite-rich granite: A case study of the Soultz-sous-Forêts geothermal site, France. *Applied Geochemistry*, *119*, 104631. https://doi.org/10.1016/j.apgeochem.2020.104631

Neal, C., & Stanger, G. (1983). Hydrogen generation from mantle source rocks in Oman. *Earth and Planetary Science Letters*, *66*, 315–320. https://doi.org/10.1016/0012-821X(83)90144-9

Normington, V. J., Hill, S. M., Tiddy, C. J., & Giles, D. (2018). *Sedimentology of the late Palaeozoic Cape Jervis Formation, Troubridge Basin, South Australia*. Department for Energy and Mining.

Nothaft, D. B., Templeton, A. S., Kelemen, P. B., Boyd, E. S., & Matter, J. M. (2026). Active conversion of atmospheric carbon dioxide to methane in peridotites of the Samail Ophiolite, Oman. *Scientific Reports*, *16*(1), 4046. https://doi.org/10.1038/s41598-025-34170-5

Onstott, T. C., Lin, L.-H., Davidson, M., Mislowack, B., Borcsik, M., Hall, J., et al. (2006). The origin and age of biogeochemical trends in deep fracture water of the Witwatersrand Basin, South Africa. *Geomicrobiology Journal*, *23*(6), 369–414. https://doi.org/10.1080/01490450600875688

Parnell, J., & Blamey, N. (2017). Global hydrogen reservoirs in basement and basins. *Geochemical Transactions*, *18*(1), 2. https://doi.org/10.1186/s12932-017-0041-4

Parry, W. T., & Downey, L. M. (1982). Geochemistry of hydrothermal chlorite replacing igneous biotite. *Clays and Clay Minerals*, *30*(2), 81–90. https://doi.org/10.1346/CCMN.1982.0300201

Potter, J., Salvi, S., & Longstaffe, F. J. (2013). Abiogenic hydrocarbon isotopic signatures in granitic rocks: Identifying pathways of formation. *Lithos*, *182–183*, 114–124. https://doi.org/10.1016/j.lithos.2013.10.001

Reid, A., Hand, M., Jagodzinski, E., Kelsey, D., & Pearson, N. (2008). Paleoproterozoic orogenesis in the southeastern Gawler Craton, South Australia. *Australian Journal of Earth Sciences*, *55*(4), 449–471. https://doi.org/10.1080/08120090801888594

Reid, A. J., Wade, C. E., & Jagodzinski, E. A. (2022). Mafic dykes of the southeastern Gawler Craton: *Ca* 1564 Ma magmatism with an enriched mantle source. *Australian Journal of Earth Sciences*, *69*(5), 711–732. https://doi.org/10.1080/08120099.2022.2014963

Rogers, A. F. (1916). Sericite: A low temperature alteration mineral. *Economic Geology*, *11*, 118-150.

Salvi, S., & Williams-Jones, A. E. (1997). Fischer-Tropsch synthesis of hydrocarbons during sub-solidus alteration of the Strange Lake peralkaline granite, Quebec/Labrador, Canada. *Geochimica et Cosmochimica Acta*, *61*(1), 83–99. https://doi.org/10.1016/S0016-7037(96)00313-4

Sherwood Lollar, B., Frape, S. K., Fritz, P., Macko, S. A., Welhan, J. A., Blomqvist, R., & Lahermo, P. W. (1993). Evidence for bacterially generated hydrocarbon gas in Canadian shield and fennoscandian shield rocks. *Geochimica et Cosmochimica Acta*, *57*(23–24), 5073–5085. https://doi.org/10.1016/0016-7037(93)90609-Z

Sherwood Lollar, B., Frape, S. K., Weise, S. M., Fritz, P., Macko, S. A., & Welhan, J. A. (1993). Abiogenic methanogenesis in crystalline rocks. *Geochimica et Cosmochimica Acta*, *57*(23–24), 5087–5097. https://doi.org/10.1016/0016-7037(93)90610-9

Sherwood Lollar, B., Onstott, T. C., Lacrampe-Couloume, G., & Ballentine, C. J. (2014). The contribution of the Precambrian continental lithosphere to global H_2 production. *Nature*, *516*(7531), 379–382. https://doi.org/10.1038/nature14017

Sherwood Lollar, B., Voglesonger, K., Lin, L.-H., Lacrampe-Couloume, G., Telling, J., Abrajano, T. A., et al. (2007). Hydrogeologic controls on episodic H_2 release from Precambrian fractured rocks—Energy for deep subsurface life on Earth and Mars. *Astrobiology*, *7*(6), 971–986. https://doi.org/10.1089/ast.2006.0096

Silver, B. J., Raymond, R., Sigman, D. M., Prokopeko, M., Sherwood Lollar, B., Lacrampe-Couloume, G., et al. (2012). The origin of NO_3^- and N_2 in deep subsurface fracture water of South Africa. *Chemical Geology*, *294–295*, 51–62. https://doi.org/10.1016/j.chemgeo.2011.11.017

Simonetti, A., Heaman, L. M., Chacko, T., & Banerjee, N. R. (2006). In situ petrographic thin section U–Pb dating of zircon, monazite, and titanite using laser ablation–MC–ICP-MS. *International Journal of Mass Spectrometry*, *253*(1–2), 87–97. https://doi.org/10.1016/j.ijms.2006.03.003

Swaraj, S., Belkhou, R., Stanescu, S., Rioult, M., Besson, A., & Hitchcock, A. P. (2017). Performance of the HERMES beamline at the carbon K-edge. *Journal of Physics: Conference Series*, *849*, 012046. https://doi.org/10.1088/1742-6596/849/1/012046

Truche, L., Bourdelle, F., Salvi, S., Lefeuvre, N., Zug, A., & Lloret, E. (2021). Hydrogen generation during hydrothermal alteration of peralkaline granite. *Geochimica et Cosmochimica Acta*, *308*, 42–59. https://doi.org/10.1016/j.gca.2021.05.048

Van Den Kerkhof, A. M., & Hein, U. F. (2001). Fluid inclusion petrography. *Lithos*, *55*(1–4), 27–47. https://doi.org/10.1016/S0024-4937(00)00037-2

Verati, C., & Jourdan, F. (2014). Modelling effect of sericitization of plagioclase on the $^{40}K/^{40}Ar$ and $^{40}Ar/^{39}$ Ar chronometers: Implication for dating basaltic rocks and mineral deposits. *Geological Society, London, Special Publications*, *378*(1), 155–174. https://doi.org/10.1144/SP378.14

Vidal, O. (2005). Thermodynamic properties of the Tschermak solid solution in Fe-chlorite: Application to natural examples and possible role of oxidation. *American Mineralogist*, *90*(2–3), 347–358. https://doi.org/10.2138/am.2005.1554

Vidal, O., Lanari, P., Munoz, M., Bourdelle, F., & De Andrade, V. (2016). Deciphering temperature, pressure and oxygen-activity conditions of chlorite formation. *Clay Minerals*, *51*(4), 615–633. https://doi.org/10.1180/claymin.2016.051.4.06

Wang, J., Morin, C., Li, L., Hitchcock, A. P., Scholl, A., & Doran, A. (2009). Radiation damage in soft X-ray microscopy. *Journal of Electron Spectroscopy and Related Phenomena*, *170*(1–3), 25–36. https://doi.org/10.1016/j.elspec.2008.01.002

Ward, L. (1933). Inflammable gases occluded in the pre-palaeozoic rocks of South Australia. *Transactions and Proceedings of the Royal Society of South Australia*, 42–47.

Warr, O., Giunta, T., Ballentine, C. J., & Sherwood Lollar, B. (2019). Mechanisms and rates of ^4He, ^{40}Ar, and H_2 production and accumulation in fracture fluids in Precambrian Shield environments. *Chemical Geology*, *530*, 119322. https://doi.org/10.1016/j.chemgeo.2019.119322

Warr, O., Song, M., & Sherwood Lollar, B. (2023). The application of Monte Carlo modelling to quantify in situ hydrogen and associated element production in the deep subsurface. *Frontiers in Earth Science*, *11*, 1150740. https://doi.org/10.3389/feart.2023.1150740

Whitcombe, J., McDonald, N., Cressey, R., Hadi Subrata, B., Falloon, S., Carr, N., & Glass, F. (2024). Ramsay 1 and Ramsay 2, learnings from the first natural hydrogen exploration wells in Australia. *Australian Energy Producers Journal*, *64*(2), S453–S458. https://doi.org/10.1071/EP23119

Wilkinson, B. H., & McElroy, B. J. (2007). The impact of humans on continental erosion and sedimentation. *Geological Society of America Bulletin*, *119*(1–2), 140–156. https://doi.org/10.1130/B25899.1

Wilner, J. A., Nordin, B. J., Getraer, A., Gregoire, R. M., Krishna, M., Li, J., et al. (2024). Limits to timescale dependence in erosion rates: Quantifying glacial and fluvial erosion across timescales. *Science Advances*, *10*(51), eadr2009. https://doi.org/10.1126/sciadv.adr2009

Zang, W. L., Fanning, C. M., Purvis, A. C., Raymond, O. L., & Both, R. A. (2007). Early Mesoproterozoic bimodal plutonism in the southeastern Gawler Craton, South Australia. *Australian Journal of Earth Sciences*, *54*(5), 661–674. https://doi.org/10.1080/08120090701305210